Aethalometer multiple scattering correction C_{ref} for mineral dust aerosols

Claudia Di Biagio[1], Paola Formenti[1], Mathieu Cazaunau[1], Edouard Pangui[1], Nicolas Marchand[2], and Jean-François Doussin[1]

[1] Laboratoire Interuniversitaire des Systèmes Atmosphériques (LISA), UMR 7583, CNRS, Université Paris Est Créteil et Université Paris Diderot, Institut Pierre et Simon Laplace, Créteil, France

[2] Aix Marseille Univ., CNRS, LCE, Marseille, France

Correspondence to: C. Di Biagio (cldibiagio@gmail.com) and P. Formenti (paola.formenti@lisa.u-pec.fr)

Abstract

In this study we provide a first estimate of the aethalometer multiple scattering correction C_{ref} for mineral dust aerosols. C_{ref} is an empirical constant used to correct the aerosol absorption coefficient measurements for the multiple scattering artefact of the aethalometer, i.e. the filter fibres on which aerosols are deposited scatter light and this is miscounted as absorption. The C_{ref} at 450 and 660 nm was obtained from the direct comparison of aethalometer data (Magee Sci. AE31) with the absorption coefficient calculated as the difference between the extinction and scattering coefficients measured by a Cavity Attenuated Phase Shift Extinction analyzers (CAPS PMex) and a nephelometer respectively at 450 nm and the absorption coefficient from a MAAP (Multi-Angle Absorption Photometer) at 660 nm. Measurements were performed on seven dust aerosol samples generated in the laboratory by the mechanical shaking of natural parent soils issued from different source regions worldwide. The single scattering albedo (SSA) at 450 and 660 nm and the size distribution of the aerosols were also measured.

C_{ref} for mineral dust varies between 1.81 and 2.56 for a SSA of 0.85–0.96 at 450 nm and between 1.75 and 2.28 for a SSA of 0.98–0.99 at 660 nm. The calculated mean and one standard deviation C_{ref} for dust is 2.09 (± 0.22) at 450 nm and 1.92 (± 0.17) at 660 nm. With this new C_{ref} the dust absorption coefficient by aethalometer is about 2% (450 nm) and 11% (660 nm) higher than that obtained by using C_{ref}=2.14 at both 450 and 660 nm, as usually assumed in the literature. This difference induces up to 3% change in the dust SSA at 660 nm. The C_{ref} seems independent of the particle fine and coarse size fractions, and so the obtained C_{ref} can be applied to dust both close to sources and following transport. Additional experiments performed with pure kaolinite mineral and polluted ambient aerosols indicate a C_{ref} of 2.49 (± 0.02) and 2.32 (± 0.01) at 450 and 660 nm respectively (SSA=0.96–0.97) for kaolinite, and a C_{ref} of 2.32 (± 0.36) at 450 nm and 2.32 (± 0.35) at 660 nm for pollution aerosols (SSA=0.62–0.87 at 450 nm and 0.42–0.76 at 660 nm).

1. Introduction

Abundant and widespread in the atmosphere, mineral dust strongly contributes to the global and regional direct radiative effect and climate forcing (Highwood and Ryder, 2014; Miller et al., 2014). Mineral dust interacts through processes of scattering and absorption with both incoming shortwave radiation and outgoing terrestrial longwave radiation (Sokolik and Toon, 1999). Currently, the evaluation of the direct effect of mineral dust and its climate implications is still limited by the knowledge of the intensity of the dust absorption in the shortwave spectral range (Miller et al., 2004; Balkanski et al., 2007; Solmon et al., 2008; Jin et al., 2016), represented by the light absorption coefficient (β_{abs}, units of Mm^{-1}). The absorption coefficient of mineral dust accounts for less than ~10-20% of its total shortwave extinction, where it shows a pronounced spectral variation (Cattrall et al., 2003; Redmond et al., 2010). The highest dust absorption occurs in the UV-VIS region of the spectrum, while it levels off to null values towards the near IR (Caponi et al., 2017). As a result, its single scattering albedo (SSA), i.e. the ratio of the aerosol scattering (β_{sca}) to extinction ($\beta_{ext}=\beta_{sca}+\beta_{abs}$) coefficient, increases from values of ~0.80-0.90 at 370 nm to values of ~0.95-0.99 at 950 nm (e.g., Schladitz et al., 2009; Redmond et al., 2010; Formenti et al., 2011; Ryder et al., 2013).

Given its relatively high SSA, mineral dust can be considered as weakly absorbing in the shortwave. This is particularly true when compared to other aerosol species, such as soot, for which the SSA in the visible may be as low as 0.2 (Bergstrom et al., 2007). Nonetheless, because of its elevated atmospheric concentration (~100-100000 μg m^{-3} close to sources and ~0.1-100 μg m^{-3} after mid– to intercontinental transport; e.g., Goudie and Middleton, 2006; Kandler et al., 2009; Querol et al., 2009; Denjean et al., 2016a), light absorption by mineral dust can be comparable to that of soot both at regional and global scales (Reddy et al., 2005; Caponi et al., 2017). Under very intense dust episodes, dust may absorb up to ~150 Wm^{-2} of incoming solar radiation (Slingo et al., 2006; di Sarra et al., 2011), inducing a remarkable warming of the atmospheric layer. This strong warming can alter the atmospheric structure and stability (Heinold et al., 2008), with a possible influence on the atmospheric dynamics and meteorological fields (Pérez et al., 2006). By its direct shortwave effect dust also affects the position of the Inter Tropical Convergence Zone, which in turn influences the Western African Monsoon and modifies the pattern and intensity of rainfall over Northern Africa and the Sahel (Yoshioka et al., 2007). Nonetheless, the extent of the dust effect and its implications critically depend on the exact amount of absorbed shortwave radiation. Solmon et al. (2008), for example, showed that a small change (5%) in the shortwave SSA of dust may modify the effect of dust on the Western African Monsoon, moving from a reduction to an increase of precipitation over the Sahel.

The accurate estimation of the dust absorption over the whole shortwave range is therefore necessary to properly assess its direct radiative effect and climate implications. One instrument used to obtain aerosol-light absorption from the UV to near IR range is the aethalometer (Magee Sci. AE31 model, Hansen et al., 1984; Arnott et al., 2005), operating at seven wavelengths in the 370–950 nm range. The aethalometer reports equivalent black carbon mass concentration but the spectral absorption by aerosols can be also calculated. Given its large spectral interval, the aethalometer has

been used in the past to investigate the spectral dependence of dust absorption (Fialho et al., 2005; Formenti et al., 2011), as well as the absorption by many aerosol types in different environments (Sandradewi et al., 2008; Segura et al., 2014; Di Biagio et al., 2016; Backman et al., 2016). General reviews on aerosol absorption measurements and their applications are provided by Horvath (1993) and Moosmüller et al. (2009).

The working principle of the aethalometer, a filter-based instrument, consists in measuring the attenuation through an aerosol-laden quartz filter according to the Beer-Lambert law, used then to derive the spectral attenuation coefficient (β_{ATT}) of the deposited particles (Hansen et al., 1984). The "true" spectral aerosol absorption coefficient (β_{abs}) is proportional but lower than β_{ATT} (Weingartner et al., 2003; Collaud Coen et al., 2010; hereinafter referred as W2003 and C2010), because β_{ATT} is enhanced by (i) aerosol scattering towards directions different from that of the detector (scattering effect); (ii) gradual accumulation of absorbing particles on the loaded filter, thus reducing the optical path (loading effect); (iii) multiple scattering of the light beam by the filter fibres, increasing the optical path (multiple scattering effect).

Empirical formulations of the scattering and loading effects are available in the literature and permit the correction of aethalometer data for these artefacts (W2003; Arnott et al., 2005; Schmid et al., 2006; Virkkula et al., 2007; C2010). The correction of the multiple scattering effect instead requires the knowledge of a correction factor C_{ref}, which needs to be directly estimated by comparison of aethalometer data against reference absorption measurements (W2003; C2010).

Currently data for C_{ref} are available for soot particles (C_{ref}=2.1-2.2 at 660 nm, W2003), internally and externally mixed soot particles and organic material (C_{ref}=2.3-3.9, W2003), and ambient aerosols collected in Europe and Amazonia (C_{ref}=2.6-4.8, C2010; C_{ref}=4.9-6.3, Saturno et al., 2016) and in the Arctic (C_{ref}=3.1, Backman et al., 2016). The value most often used in the literature is 2.14 (± 0.21), assumed as wavelength-independent (e.g., Sandradewi et al., 2008; Formenti et al., 2011; Di Biagio 2016), which corresponds to the mean of observations at 660 nm for soot aerosols (W2003). Both W2003 and C2010, however, found a dependence of C_{ref} on the aerosol single scattering albedo, with C_{ref} decreasing for increasing SSA. Thus, the value of 2.14 obtained for highly absorbing soot (SSA~0.2 in the visible) may not be appropriate for weakly absorbing mineral dust.

Henceforth, in this work we present the experimental estimate of C_{ref} for mineral dust aerosols at 450 and 660 nm obtained from a laboratory-based intercomparison study. Experiments were conducted on seven dust aerosol samples generated by the mechanical shaking of natural parent soils. Control experiments on pure kaolinite mineral, ambient aerosols sampled in the polluted environment of the suburbs of Paris, and purely scattering ammonium sulfate, were also performed to investigate the dependence of C_{ref} on the aerosol single scattering albedo.

2. Experimental set-up

The experimental set-up used for the intercomparison study is shown in **Fig. 1**. Instrumental details and uncertainties are summarized in **Table 1**. The following measurements were performed from a 8-port glass manifold (~1 L volume):

- the absorption coefficient (β_{abs}) by a 7-wavelength aethalometer (Magee Sci., model AE31 working at 370, 470, 520, 590, 660, 880, 950 nm; flowrate 8 L min^{-1}, 2-min resolution) and a MAAP (Multi-Angle Absorption Photometer, Thermo Sci., model 5012 working at 670 nm; flowrate 8 L min^{-1}, 1-min resolution). Unlike the aethalometer, the MAAP measures the transmitted light from the aerosol-laden filter and also the backscattered light at two angles (135° and 165°) (Petzold et al., 2005). Backscattering measurements are used to constrain the scattering fraction of the measured attenuation that would erroneously be interpreted as absorption. The aerosol absorption coefficient for the MAAP is obtained from a radiative transfer scheme taking into account the multiple scattering in the filter and the scattering effect, without requiring any further adjustment (Petzold and Schönlinner, 2004). The MAAP is commonly assumed to provide the most reliable filter–based direct estimate of the aerosol absorption coefficient at a single wavelength (Andreae and Gelècser 2006). In this study we assume for the MAAP the manufacturer's reported wavelength of 670 nm, although Müller et al. (2011) measured for this instrument a wavelength of 637 nm. An estimate of the change in the obtained C_{ref} due to the change in MAAP nominal wavelength from 670 to 637 nm is reported in Sect. 4.2;

- the scattering coefficient (β_{sca}) in the 7-170° angular range by a 3-wavelength nephelometer (TSI Inc., model 3563 working at 450, 550 and 700 nm; flowrate 18 L min^{-1}, 1-s resolution);

- the extinction coefficient (β_{ext}) by two Cavity Attenuated Phase Shift Extinction analyzers (CAPS PMex by Aerodyne, one working at 450 nm and the other at 630 nm; flowrate 0.85 L min^{-1}, 1-s resolution);

- the particle number size distribution (dN/dlogD) by a scanning mobility particle sizer, SMPS, (TSI Inc., DMA Model 3080, CPC Model 3772; operated at 2.0/0.2 L min^{-1} sheath/aerosol flow rates; 3-min resolution) and an optical particle counter, OPC, (Grimm Inc., model 1.109, 655 nm operating wavelength; flowrate 1.2 L min^{-1}, 6-s resolution). The SMPS measures the aerosol number concentration in the electrical mobility diameter (D_m) range 0.019–0.882 μm, and the OPC measures in the optical equivalent diameter (D_{opt}) range 0.25-32 μm.

Sampling lines from the manifold to the instruments were made of conductive silicone tubing (TSI Inc., $6.4 \cdot 10^{-3}$ m diameter) to minimize particle loss by electrostatic deposition. They were designed to be as straight and as short as possible. Their length, varying between 0.3 and 0.7 m, was adjusted based on the flowrate of each instrument to ensure an equivalent particle loss, so that the same aerosol size distribution was in input to the different instruments. Particular care was given to ensure the same aerosol size at the input of the aethalometer and the MAAP. To this end, as illustrated in Fig. 1, the two instruments sampled air from the same manifold exit line, and also the same sampling flow rate was set for the two instruments (8 L min^{-1}). Particle loss calculations were performed with the Particle Loss Calculator (PLC) software (von der Weiden et al., 2009).

Aerosols were generated in three ways:

- mineral dust was generated by mechanical shaking as described and validated in Di Biagio et al. (2014, 2017). About 3 gr of soil sample (sieved at 1000 μm and dried at 100°C) was placed in a

Büchner flask and shaken at 100 Hz by a sieve shaker (Retsch AS200). The dust was injected in the manifold by a flow of N_2 at 3.5 L min^{-1} through a single-stage impactor used to eliminate particles larger than about 20 µm, which could be preferentially sampled by the instruments with the highest flow rate. Pure N_2 was added to the aerosol flow to make the injection flow equal to the total sampling flow by instruments connected to the manifold (about 38 L min^{-1});

- ammonium sulfate (Sigma-Aldrich 99.999% purity, 0.03 M solution in ultrapure water) and kaolinite particles (Source Clay Repository KGa-2, 0.05 M solution in ultrapure water) were generated by a constant flow atomizer (TSI, model 3075) operated at 3 L min^{-1} and coupled with a diffusion drier (TSI, model 3062). As for dust, pure N_2 was added to the aerosol flow to equalize the total sampling flow;

- ambient pollution aerosols were sampled by opening the manifold to the exterior ambient air. Ambient aerosols were not dried before entering the manifold. Sampling was performed at the University Paris-Est Creteil, in the suburbs of Paris, at the ground floor of the University building, which is close to a main local road (~20 m) and to the A86 highway (~200 m).

3. Strategy for data analysis

The aethalometer spectral attenuation coefficient $\beta_{ATT}(\lambda)$ is related to the measured attenuation ATT(λ) through the following formula:

$$\beta_{ATT}(\lambda) = \frac{\Delta ATT(\lambda)}{\Delta t}\frac{A}{V} \quad (1)$$

where A is the area of the aerosol collection spot (0.5 ± 0.1) cm^2 and V the air sampled volume (0.016 m^3 over 2-min integration time). ΔATT(λ)/Δt in Eq. (1) can be calculated as the linear fit of the measured attenuation as a function of time.

The spectral attenuation coefficient $\beta_{ATT}(\lambda)$ measured by the aethalometer is related to the targeted absorption coefficient $\beta_{abs}(\lambda)$ by the following formula (C2010):

$$\beta_{abs}(\lambda) = \frac{\beta_{ATT}(\lambda) - \alpha(\lambda)\beta_{sca}(\lambda)}{R \cdot C_{ref}} \quad (2)$$

where the different terms parametrise different instrument artefacts:

- the scattering effect $\alpha(\lambda)\beta_{sca}(\lambda)$, that is, the amount of scattered radiation by the aerosols deposited on the filter that is miscounted as absorption, where α(λ) is a wavelength-dependent proportionality constant and $\beta_{sca}(\lambda)$ is the aerosol spectral scattering coefficient;

- the loading effect R, representing the artificial flattening of measured attenuation with time due to the gradual accumulation of absorbing particles on the loaded filter;

- the multiple scattering C_{ref}, representing multiple scattering of the light beam by the filter fibres.

The α(λ) term and R in Eq. (2) can be calculated through various empirical formulas reported in the literature (W2003, Arnott et al., 2005; Virkkula et al., 2007; Schmid et al., 2006; C2010). The determination of C_{ref},instead, is the objective of our study.

3.1. Scattering effect correction

Arnott et al. (2005) provide for $\alpha(\lambda)$ the following formulation:

$$\alpha(\lambda)=A^{d-1}\cdot c\cdot\lambda^{-\alpha_S(d-1)} \quad (3)$$

where the A and α_S terms are obtained from the power-law fit of $\beta_{sca}(\lambda)$ versus λ, and the c and d terms can be determined from the power-law fit of the attenuation $\beta_{ATT}(\lambda)$ versus the scattering $\beta_{sca}(\lambda)$ coefficient as

$$\beta_{sca}(\lambda)=A\lambda^{-\alpha_S} \quad (4)$$

$$\beta_{ATT}(\lambda)=c\beta_{sca}(\lambda)^{d} \quad (5)$$

3.2. Loading effect correction

Two formulations for the loading effect correction R are proposed by W2003 and C2010:

$$R(W2003)(\lambda)=\left(\frac{1}{f(\lambda)}-1\right)\frac{\ln(ATT(\lambda))-\ln(10\%)}{\ln(50\%)-\ln(10\%)}+1 \quad (6a)$$

$$R(C2010)(\lambda)=\left(\frac{1}{f(\lambda)}-1\right)\frac{ATT(\lambda)}{50\%}+1 \quad (6b)$$

The factor $f(\lambda)$ represents the dependence of the loading effect on the aerosol absorption. This dependence is parametrized by the aerosol single scattering albedo $SSA(\lambda)$ in the form of

$$f(\lambda)=a\left(1-SSA(\lambda)\right)+1 \quad (7)$$

where *a*, equal to 0.85 in W2003 and 0.74 in C2010, is obtained as the slope of the linear fit between the attenuation coefficient β_{ATT} normalized to its value at 10% attenuation ($\beta_{ATT}/\beta_{10\%}$) and the natural logarithm of the measured attenuation $\ln(ATT(\lambda))$.

3.3. Multiple scattering correction

For the determination of C_{ref} only β_{ATT} and R are required. Henceforth in this work, attenuation data from the aethalometer were corrected for the loading effect R but not for the scattering term $\alpha(\lambda)\beta_{sca}(\lambda)$. Three different formulations of C_{ref} were therefore considered:

$$C_{ref}^{*}(\lambda)=\frac{\beta_{ATT}(\lambda)}{\beta_{abs\text{-}ref}(\lambda)} \quad (8a)$$

$$C_{ref}(W2003)(\lambda)=\frac{1}{\beta_{abs\text{-}ref}(\lambda)}\frac{\beta_{ATT}(\lambda)}{R(W2003)(\lambda)} \quad (8b)$$

$$C_{ref}(C2010)(\lambda)=\frac{1}{\beta_{abs\text{-}ref}(\lambda)}\frac{\beta_{ATT}(\lambda)}{R(C2010)(\lambda)} \quad (8c)$$

The $\beta_{abs\text{-}ref}$ term in Eq. 8a-8c represents the reference absorption coefficient estimated from independent measurements. C_{ref}^{*} does not take into account the loading effect correction in aethalometer data, as done by Schmid et al. (2006). C_{ref}(W2003) and C_{ref}(C2010) take this correction into account, by using the R(W2003) and the R(C2010) parametrisations, respectively. The spectral β_{ATT}/R(C2010) was used to calculate the absorption Ángström exponent (α_A). Note that in this work we considered, for each experiment, only data corresponding to ATT < 20% to calculate β_{ATT} (R^2>0.99 for the $\Delta ATT/\Delta t$ fits in all cases, see Eq. (1)). This threshold was fixed based on two requirements: first, we limited our data analysis to points with low attenuation in order to account almost exclusively for the scattering by the filter fibers in the C_{ref} calculation and not for the scattering from aerosol particles embedded in the filter. This choice was done also for consistency with the literature, since both W2003 and C2010 relate C_{ref} to ATT~10%. Second, this choice ensured that enough data points were available for analysis regardless of the aerosol type, in particular for ambient aerosols, for which attenuation rapidly exceeded 10%.

3.4. Determination of reference absorption coefficient and single scattering albedo

The reference absorption coefficient $\beta_{abs\text{-}ref}$ in Eq. 8a-8c was obtained in different ways depending on wavelength. At 450 nm, $\beta_{abs\text{-}ref}$ was obtained with the “extinction minus scattering” approach by using the CAPS measurements for extinction and the nephelometer measurements for scattering. At 660 nm, $\beta_{abs\text{-}ref}$ was extrapolated from MAAP measurements at 670 nm.

3.4.1. Direct determination of reference absorption coefficient at 660 nm from the MAAP

The reference absorption coefficient $\beta_{abs\text{-}ref}$ at 660 nm was obtained by the MAAP measurement at 670 nm. The MAAP attenuation (ATT) at 670 nm is estimated from the measured transmission (T) and retrieved single scattering albedo of the aerosol-filter layer (SSA_0, from the inversion algorithm) as

$$ATT(670) = (1 - SSA_0) \cdot \ln T \cdot 100 \quad (9)$$

Equation (1) is applied to estimate the absorption coefficient at 670 nm from ATT(670). The area of the aerosol collection spot is 2 cm^2 and the sampled volume is 0.008 m^3 over 1-min integration time. The absorption coefficient of the MAAP was extrapolated to the 660 nm wavelength by using the absorption Ángström exponent α_A calculated from aethalometer data.

3.4.2. Indirect determination of reference absorption coefficient at 450 nm: "extinction minus scattering” approach

The reference absorption coefficient $\beta_{abs\text{-}ref}$ at 450 nm was calculated as the difference between the extinction and scattering coefficient from the CAPS and the nephelometer.

The extinction coefficient β_{ext} at 450 and 630 nm was measured directly by the two CAPS analyzers without additional corrections (Massoli et al., 2010). The spectral β_{ext} was used to calculate the extinction Ángström exponent (α_E), applied then to extrapolate β_{ext} at 660 nm.

The scattering coefficient β_{sca} at 450, 550, and 700 nm measured by the nephelometer between 7 and 170° was corrected for the size-dependent angular truncation of the sensing volume to report it to the full angular range 0°-180° (Anderson and Ogren, 1998). Two different approaches were used: for sub-micrometric ammonium sulfate, the correction proposed by Anderson and Ogren (1998) was applied, while for aerosols with a significant coarse fraction (dust, ambient air and kaolinite), the truncation correction was estimated by optical calculations according to the Mie theory for homogeneous spherical particles using as input the measured number size distribution. In the calculations the real and the imaginary parts of the complex refractive index m (m=n-*i*k, where n is the real part and k is the imaginary part) were varied in the wide range 1.42–1.56 and 0.001–0.025*i* for dust (Di Biagio et al., 2017), and 1.50–1.72 and 0.001–0.1*i* for ambient air (Di Biagio et al., 2016), while the value of 1.56-0.001*i* was assumed for kaolinite (Egan and Hilgeman, 1979; Utry et al., 2015). Then, n and k were set to the values which reproduced the measured β_{sca} at 7-170°. The truncation correction factor (C_{trunc}) was estimated as the ratio of the modelled β_{sca} at 0°-180° and 7°-170°. At the three nephelometer wavelengths (450, 550, and 700 nm) the correction factor C_{trunc} varied in the range 1.03-1.06 for ammonium sulfate, 1.08-1.6 for dust, 1.03-1.05 for kaolinite, and 1.05-1.25 for ambient air. For both approaches (Anderson and Ogren (1998) correction and Mie calculations) the uncertainty on the truncation correction was estimated to be less than 3%. Once corrected for truncation, the spectral β_{sca} was used to calculate the scattering Ångström exponent (α_S), which was then applied to extrapolate β_{sca} at 630 and 660 nm.

3.4.3. Determination of the single scattering albedo (SSA)

The aerosol single scattering albedo (SSA) represents the ratio of scattering to extinction. At 450 nm, the SSA was estimated by nephelometer and CAPS data (Eq. 10), while at 660 nm CAPS data were combined with MAAP observations (Eq. 11):

$$SSA(450)=\frac{\beta_{sca}(450)_{nephelometer}}{\beta_{ext}(450)_{CAPS}} \quad (10)$$

$$SSA(660)=\frac{\beta_{ext}(660)_{CAPS}-\beta_{abs-MAAP}(660)}{\beta_{ext}(660)_{CAPS}} \quad (11)$$

3.5. Number size distribution and effective fine and coarse diameter

The number size distribution was measured by a combination of SMPS and OPC observations. For the SMPS, corrections for particle loss by diffusion in the instrument tubing and the contribution of multiple-charged particles were performed using the SMPS software. The electrical mobility diameter measured by the SMPS can be converted to a geometrical diameter (D_g) by taking into account the particle dynamic shape factor (χ; $D_g=D_m/\chi$). In this study, the SMPS showed a good agreement with OPC data for a shape factor χ=1, which corresponds to spherical particles.

The OPC optical-equivalent nominal diameters were converted into sphere-equivalent geometrical diameters (D_g) by taking into account the aerosol complex refractive index. This consisted in recalculating the OPC calibration curve for different complex refractive index values. For dust

aerosols the refractive index was varied in the range 1.47-1.53 (n) and 0.001-0.005*i* (k) following the literature (see Di Biagio et al., 2017) and D_g was set at the mean ± one standard deviation of the values obtained for the different n and k. For kaolinite the OPC diameter conversion was performed by setting the refractive index at 1.56-0.001*i*. For ambient air the refractive index was set at 1.60-0.01*i*, a value that represents a medium absorbing urban polluted aerosol (see Di Biagio et al., 2016). The impact of humidity on the refractive index of ambient aerosols and associated changes OPC response were not taken into account. The relative humidity was always below 35% during ambient air measurements, which implies a very small particle growth. After conversion, the OPC diameter range became 0.28-18.0 μm for dust (taking into account the particle cut at ~20 μm due to the use of the impactor), and 0.27-58.0 μm for kaolinite and 0.28-65.1 μm for ambient air (the impactor was not used in these cases). The uncertainty was <15% at all diameters.

The aerosol effective fine ($D_{eff,fine}$) and coarse ($D_{eff,coarse}$) diameter were estimated from OPC data as

$$D_{eff} = \frac{\int_{D_1}^{D_2} D_g^3 \frac{dN}{dlogD_g} dlogD_g}{\int_{D_1}^{D_2} D_g^2 \frac{dN}{dlogD_g} dlogD_g} \quad (12)$$

with D_1=0.3 μm and D_2=1 μm for the fine mode and D_1=1 μm and D_2=10 μm for the coarse mode.

3.6. Data integration and error analysis

Aethalometer data were first processed at 2-min resolution to obtain the time evolution of the attenuation coefficients β_{ATT} and β_{ATT}/R. Data from the MAAP, CAPS, nephelometer, OPC and SMPS were averaged over 2-min to report them to the same resolution of the aethalometer.

Then the β_{ATT} and β_{ATT}/R were calculated over the whole duration of each experiment from Eq. (1) and (6). Corresponding averages of the reference absorption coefficient ($\beta_{abs\text{-}ref}$) were calculated for each experiment and used to estimate C_{ref}. Experiment-averages of SSA, $D_{eff,fine,}$ and $D_{eff,coarse}$ were also calculated to relate to the obtained C_{ref}.

The uncertainty of C_{ref} was estimated with the error propagation formula by taking into account the uncertainties on β_{ATT}, β_{ATT}/R, and the standard deviation of the averaged $\beta_{abs\text{-}ref}$ from the CAPS-nephelometer and the MAAP. The uncertainty of β_{ATT} was estimated as the quadratic combination of the uncertainty of the linear fit of ΔATT with respect to time and the uncertainties on the surface deposit A. The uncertainty of β_{ATT}/R was estimated taking into account the uncertainty of β_{ATT} and R. Uncertainties on β_{ATT} and β_{ATT}/R are both ~20%.

4. Results

The time series of observations for all the experiments are shown in **Fig. 2** as 2-min averages. Seven experiments were performed on mineral dust issued from six different areas in the Sahel (Niger), Eastern Asia (China), North America (Arizona), Northern Africa (Tunisia), Australia, and Southern Africa (Namibia), and on a kaolinite powder. Experiments were performed between the 3rd and the 9th of November 2016 and lasted between 1 and 2 hours each. The experiment on Niger dust (labelled as Niger 1 and Niger 2) were duplicated to test the repeatability of the obtained C_{ref}. Ambient air data

were collected between the 8th and the 14th November 2016 for a total of 7 hours of measurements. Eight different periods characterized by little variation and different levels of SSA were selected in the whole set of ambient air measurements. These are identified as ambient air 1 to 8. The summary of information is provided in **Table 2**. SMPS data were available for ammonium sulfate and kaolinite experiments, for one of the two Niger dust experiments (Niger 2), and for some of the ambient air experiments. OPC measurements were performed for all experiments with the exception of the ammonium sulfate.

4.1. Quality control data

Results of the ammonium sulfate control experiment (24 October 2016), used to test the performance of the optical instruments, are illustrated in **Fig. 3**. As expected for this purely scattering aerosol (Toon et al., 1976), the nephelometer scattering and the CAPS extinction at 450 and 630 nm were in very good agreement (less than 4% difference) during the whole duration of the experiment. This is well below the single instrument uncertainty of ±9% for the nephelometer (Sherman et al., 2015) and ±5% for the CAPS (Massoli et al., 2010). This is further demonstrated by the scatterplot of their respective 10-minute averages, yielding a linear regression in the form of y=0.95x+5.1 (R^2=0.95) at 450 nm and y=1.01x-1.4 (R^2=0.98) at 630 nm. The average β_{ext} at 450 and 630 nm from CAPS observations was 913 (± 52) and 424 (± 33) Mm^{-1}, respectively, while the average β_{sca} was 921 (± 36) and 420 (± 17). This led to an average SSA of 1.01 (± 0.07) at 450 nm and 0.99 (± 0.07) at 630 nm.

The absorption coefficient, averaged over the duration of the experiment, was 0.10 (± 0.04) Mm^{-1} at 450 nm and 0.24 (± 0.07) Mm^{-1} at 660 nm according to the aethalometer, and 0.82 (± 0.13) Mm^{-1} at 660 nm according to the MAAP. For the aethalometer, the absorption coefficient was calculated from Eq. (2) assuming C_{ref}=2.14 and the R formulation by C2010 (Eq. 6b). The α(λ) coefficient was calculated from Eq. (3). The c and d terms in Eq. (3) were determined from the power-law fit of $\beta_{ATT}(\lambda)$ vs $\beta_{sca}(\lambda)$ and are c=(0.56 ± 0.06) Mm^{-1} and d=(0.485 ± 0.09). These values are lower than those reported by Arnott et al. (2005) (c=0.797, d=0.564). The A and α_S terms, obtained from the power law fit of $\beta_{sca}(\lambda)$ vs wavelength (Eq. 3) are A=(4.07 ± 0.49)10^9 Mm^{-1} and α_S=(-2.46 ± 0.12).

Figure 4 shows the extinction coefficient at 660 nm extrapolated from CAPS observations and calculated as the sum of nephelometer and MAAP data for dust, kaolinite, and ambient air experiments. The linear regression of the data yields y=1.03x-0.5 (R^2=0.99), indicating the consistency of optical measurements between the CAPS, nephelometer, and MAAP (less than 3% difference on average). Based on the success of the optical closure at 660 nm, we therefore assume the "CAPS minus nephelometer" approach appropriate to estimate the aerosol absorption coefficient at 450 nm.

4.2. Estimate of C_{ref}

The C_{ref}^*, C_{ref}(W2003) and C_{ref}(C2010) at 450 and 660 nm obtained for all different experiments and the corresponding aerosol SSA, $D_{eff,fine}$, and $D_{eff,coarse}$ are summarized in **Table 2**.

C_{ref} for mineral dust varied between 1.81 and 2.56 for a SSA of 0.85–0.96 at 450 nm and between 1.75 and 2.28 for a SSA of 0.98–0.99 at 660 nm. The estimate for Niger 1 and 2 samples agreed

within 4.9%, which suggests a good repeatability of the C_{ref} estimate. For kaolinite C_{ref} was 2.47–2.51 and 2.31–2.34 at 450 and 660 nm, respectively, with an associated SSA of 0.96 and 0.97 at the two wavelengths. For ambient air C_{ref} varied in the range 1.91–4.35 for a SSA of 0.62–0.87 at 450 nm and 1.66–2.96 for and SSA of 0.42–0.76 at 660 nm. For samples 6 and 8 the C_{ref} at 450 was lower than at 660 nm. Otherwise, for all other cases, the C_{ref} was larger at 450 nm than at 660 nm.

Differences within 2.8% were obtained between C_{ref}^{*}, C_{ref}(W2003) and C_{ref}(C2010) at 450 and 660 nm for weakly-absorbing dust and kaolinite. In contrast, for more absorbing ambient air aerosols the differences between C_{ref}^{*}, C_{ref}(W2003) and C_{ref}(C2010) were in the range 2.7% to 24.3%. The different ATT threshold assumed here (20%) compared to W2003 and C2010 (10%) has a negligible impact (less than 1% difference) on the results. In some cases (ambient air 1–2 and Niger 1 samples), however, we obtained C_{ref}(C2010)>C_{ref}(W2003); these cases correspond to a mean aethalometer measured ATT<10%, for which R(W2003)>R(C2010), and this explains the larger C_{ref}(C2010). Conversely, C_{ref}(C2010)<C_{ref}(W2003) when the measured ATT was ~15-20%, yielding R(W2003)<R(C2010). The percent difference between the obtained C_{ref}(W2003) and C_{ref}(C2010) increased for decreasing SSA due to the increase of the R(W2003) to R(C2010) absolute difference for decreasing SSA. When averaging data for all ambient air samples, the two formulations yield very similar values. For example, at 660 nm the mean C_{ref}(W2003) was 2.44 (± 0.38), less than 2% larger than the mean C_{ref}(C2010) of 2.39 (± 0.35).

The mean and standard deviation of the multiple scattering correction at 450 and 660 nm for dust, kaolinite, and ambient air calculated as the mean of the C_{ref}^{*}, C_{ref}(W2003), and C_{ref}(C2010) are reported in **Table 3**. The mean C_{ref} at 450 and 660 nm is 2.09 (± 0.22) and 1.92 (± 0.17) for dust, 2.49 (± 0.02) and 2.31 (± 0.02) for kaolinite, and 2.32 (± 0.36) and 2.32 (± 0.35) for pollution aerosols. If the wavelength of 637 nm is assumed for the MAAP instead of 670 nm, as suggested by Müller et al. (2011), the average C_{ref} at 660 nm would increase by up to ~15% for dust and ambient air (2.17±0.19 and 2.48±0.41, respectively) and ~3% for kaolinite (2.40±0.02).

4.3. Dependence of C_{ref} on SSA

As reported in Table 2, very different SSA values at 450 and 660 nm were obtained for the various cases. For dust aerosols, the measured SSA values were larger than 0.85 at 450 nm and close to unity (>0.98) at 660 nm, in line with field observations of dust from different sources (Schladitz et al., 2009; Formenti et al., 2011; Ryder et al., 2013). In particular, our results for China, Arizona, and Australia samples are in line with published values by Engelbrecht et al. (2016), who used a photoacoustic instrument to measure absorption of re–suspended dust aerosols. This would suggest the similar performances of the aethalometer compared to the photoacoustic technique. The SSA for kaolinite was 0.96–0.97 at 450 and 660 nm, in agreement with Utry et al. (2017) also using a photoacoustic mehod to measure absorption (0.97 and 0.99 (±0.04) at 450 and 635 nm, respectively). Both at 450 and 660 nm, the single scattering albedo for ambient air varied in the wide range 0.2 to 0.9 during the whole measurement period (see Fig. 2 for measurements at 660 nm). The average values obtained for air samples 1–8 were 0.62–0.87 at 450 and 0.42–0.76 at 660 nm. The SSA decreased with increasing wavelength, as expected for pollution aerosols (e.g., Bergstrom et al.,

2007; Di Biagio et al., 2016). The wide range of values indicates the occurrence of particles with very different absorption properties, henceforth chemical composition (or complex refractive index) and/or different size distribution (e.g., Moosmüller and Arnott, 2009). For instance, in urban environments, Bergstrom et al. (2007) reported SSA in the range 0.2–1.0 at 550 nm, with lowest values observed for soot-dominated air masses and highest values for urban pollution dominated by low-absorbing organic components.

The experimental SSA values serve two purposes. First, as shown in **Fig. 5**, they are linearly related to the factor f in the loading effect correction term R in Eq. (6a)-(6b) as f=*a*(1-SSA)+1. The linear regression of our data yields a slope *a*=(1.48 ± 0.14), larger than the value of 0.85 reported in W2003 (f data from W2003 are also shown in Fig. 5) and 0.76 in C2010.

Secondly, SSA data serve to investigate the dependence of C_{ref} on relative amounts of particle absorption for mineral dust. As shown in **Fig. 6** (top panel), C_{ref} for dust seems to be independent of SSA at 660 nm, whereas it decreases for increasing SSA at 450 nm. This trend is statistically significant (correlation coefficient of R^2=0.85). The relationship between C_{ref} and SSA is also investigated in **Fig. 6** (bottom panel) for all aerosol samples. Globally, Fig. 6 suggests a decrease of C_{ref} for increasing SSA, in particular at 450 nm, albeit with a poorer statistical significance at both wavelengths (R^2=0.35 and 0.59). Data are also compared to those reported in W2003 and C2010 at 660 nm for different aerosol types. Diesel soot and soot mixed with ammonium sulfate were investigated in W2003, while C2010 reported data for ambient aerosols sampled at different locations in Europe and in Amazonia. W2003 also reported the C_{ref} for soot particles at 450 nm (not shown in Fig. 6), with values between 2.08 and 3.64; these values are in line with our observations at 450 nm for ambient air. Whereas, as illustrated in Fig. 6, both W2003 and C2010 found a relationship between C_{ref} and SSA at 660 nm, contrasting results are obtained when plotting the two datasets together. C2010 obtained a sharp and almost linear decrease of C_{ref} with increasing SSA (C_{ref}~5–2.5 for SSA~0.65–0.9), while W2003 data showed a pronounced decrease of C_{ref} (~2–4) for increasing SSA in the range 0.5 and 0.7 and low C_{ref} values (~2) at SSA~0.2. Our data for dust and kaolinite at high SSA (>0.97) seem to follow the same linear relationship as C2010. However at lower SSA, our data for ambient aerosols are closer to W2003 results at 660 nm. These differences between W2003 and C2010 data, and also with our results, are quite difficult to explain. The main difference between W2003 compared to C2010 is that W2003 performed measurements in a simulation chamber, while C2010 was a field study. Working in ambient conditions may influence the retrieved C_{ref}. In fact, volatile-organic compounds or water vapor present in the atmosphere may condense on the filter (Lack et al., 2008), thus enhancing the scattering from the filter fibers and leading to higher C_{ref}. This could explain the higher C_{ref} obtained in C2010 compared to W2003. Our results for ambient air particles, however, are in agreement with W2003 chamber results. Differences in the size distributions of the investigated aerosols are also expected to possibly affect the comparison; however, no detailed information on the size of investigated aerosols is provided in W2003 and C2010. Another source of discrepancy may be in the fact that, differently from W2003 and our study, where aethalometer and MAAP were compared at 660 nm, C_{ref} in C2010 was estimated by comparing aethalometer data at

660 nm with MAAP observations at 630 nm. As aerosol absorption increases with decreasing wavelength, this wavelength difference may induce an underestimation of C_{ref} in C2010.

4.4. Dependence of C_{ref} on particles size

Examples of the number size distribution measured by the SMPS and OPC for ammonium sulfate, Niger dust, kaolinite, and ambient air are shown in **Fig. 7**. Ammonium sulfate had mostly a submicron distribution, while dust aerosols presented the largest fraction over the whole super-micron range up to about 10-20 µm. Dust particles larger than 20 µm were completely suppressed by the impactor system and were not detected by the OPC. The coarse component, up to about 10 µm, was also identified in the kaolinite and ambient air samples. In particular, a defined mode at ~4 µm was detected in the number distribution of ambient air particles, and may be linked to the presence of soot-aggregates, tire abrasions, re-suspended road dust, or bioaerosols (Harrison et al., 2001; Bauer et al., 2008; Pakbin et al., 2010; Liu and Harrison, 2011). The $D_{eff,fine}$ varied between 0.24 and 0.62 µm and the $D_{eff,coarse}$ between 2.3 and 6.2 µm for the different cases (Table 2). For mineral dust, $D_{eff,coarse}$ ranged between 2.3 and 3.6 µm, encompassing the value of $D_{eff,coarse}$ ~ 3 µm reported by Denjean et al. (2016b) in their figure 11 for Saharan dust both close to sources and during transport over the Atlantic.

These observations are consistent with the extinction (α_E) and the absorption (α_A) Ángstrom exponent measured during the experiments. The α_E (shown in Fig.2) was ~0 for kaolinite, varied between about 0 and 2 for mineral dust aerosols, and between 0.5 and 2.5 for ambient air, indicating particles with variable sizes, both the sub-micron and the super-micron fractions. The absorption Ångström coefficient α_A obtained from aethalometer data was between 2.2 and 4 for dust, between 1 and 1.5 for kaolinite and between 0.5 and 1.5 for ambient air aerosols.

The dependence of C_{ref} at 450 and 660 nm on the effective diameter fine $D_{eff,fine}$ and coarse $D_{eff,coarse}$ as a measure of particle size was investigated. The scatterplot of C_{ref} versus $D_{eff,coarse}$ is shown in **Fig. 8** and indicates that the C_{ref} does not have any statistically significant dependence on the particle size for mineral dust at both wavelengths and for all data at 660 nm ($R^2 \leq 0.40$). Conversely, a slight increase of C_{ref} for increasing $D_{eff,coarse}$ is obtained at 450 nm when all aerosol samples are considered ($R^2=0.70$). In contrast, no dependence of C_{ref} on $D_{eff,fine}$ is found ($R^2 \leq 0.44$, not shown).

5. Conclusions

In this paper we presented an intercomparison study between an aethalometer and a MAAP, a nephelometer, and two CAPS with the aim of determining a two-wavelength multiple scattering correction (C_{ref}) for aethalometer measurements for weakly-absorbing mineral dust aerosols. Mineral dust aerosols investigated here were generated from natural parent soils collected in desert areas, both in the Northern and in the Southern hemisphere (Di Biagio et al., 2014; 2017). The size distribution of the generated dust included both the submicron and the supermicron fractions, with an effective fine and coarse diameter between 0.32–0.55 and 2.3–3.6 µm, respectively.

The estimated C_{ref} was in the range 1.81–2.56 at 450 nm and 1.75–2.28 at 660 nm for the different dust samples, with mean C_{ref} values of 2.09 (± 0.22) and 1.92 (± 0.17), respectively. Using these

values of C_{ref}, the dust absorption coefficient estimated by the aethalometer will be about 2% (450 nm) and 11% (660 nm) higher than obtained by using the wavelength-independent value of 2.14, commonly used in the literature (e.g., Sandradewi et al., 2008; Formenti et al., 2011; Di Biagio 2016). The new estimate of C_{ref} has a negligible impact on the dust SSA at 450 nm (less than 0.5% difference between the value obtained for C_{ref}=2.09 or 2.14), but affects by up to ~3% the estimate of SSA at 660 nm.

Given that the median of the solar spectrum occurs at about 700 nm, the expected change in the dust SSA at 660 nm may significantly affect the impact of dust on radiation. Mallet et al. (2009) estimated that about a 3% change in the visible SSA of dust may determine up to a 10% change in the radiative effect of dust at the surface, and up to 20% change at the Top of the Atmosphere, with a net ~25% increase of dust absorption in the atmosphere. Given the strong sensitivity of the dust direct effect to particle absorption (Solmon et al., 2008; Mallet et al., 2009; Di Biagio et al., 2010; Jin et al., 2016, among others), we recommend this new C_{ref} value at 660 nm to be used when analyzing aethalometer data for mineral dust aerosols.

The analysis performed in this study indicates that there is no dependence of C_{ref} on the coarse component of the particle size distribution for dust. This suggests that the C_{ref} obtained here can be used to correct aethalometer data for dust at emission, when the coarse fraction dominates the dust size distribution, as well as after long-range transport, when the coarsest component of dust has preferentially settled out.

Finally, our body of observations, spanning a wide range of SSA values from 0.96–0.97 (kaolinite) to ~0.4–0.8 (ambient urban aerosols), indicates that C_{ref} decreases for increasing SSA, both at 450 and 660 nm. This is generally consistent with the results of W2003 and C2010 at 660 nm. However, a unique relationship cannot be established. At high SSA (>0.90), our data, as well as those of C2010, suggest a sharper decrease than at SSA in the range 0.4-0.8, where our data are more consistent with those of W2003. Differences in aerosol sampling conditions and in the exact analysed wavelengths from the three studies may be the cause of such discrepancy, but clear conclusions, as well as an explicit relationship between C_{ref} and SSA, are still difficult to give. Similarly, our observations seem to indicate that C_{ref} increases for increasing $D_{eff,coarse}$ at 450 nm. This trend was only observed when the entire dataset was considered, but not if the dataset was limited to just the dust observations, making it difficult to draw clear conclusions.

A more extensive characterization of C_{ref} is required to provide an appropriate correction of aethalometer data under the wide range of atmospheric conditions.

Data availability

Experimental and processed data are available upon request to the contact author.

Author contributions

C. Di Biagio and P. Formenti designed the experiments, discussed the results, and wrote the manuscript with comments from all co-authors. N. Marchand provided the MAAP used in the

experiments. C. Di Biagio, M. Cazaunau, and E. Pangui performed the experiments. C. Di Biagio performed the data analysis.

Competing interests

The authors declare that they have no conflict of interest.

Acknowledgements

The RED-DUST project was supported by the French national programme LEFE/INSU, by the Institut Pierre Simon Laplace (IPSL), and by OSU-EFLUVE (Observatoire des Sciences de l'Univers-Enveloppes Fluides de la Ville à l'Exobiologie) through dedicated research funding. C. Di Biagio was supported by the CNRS via the Labex L-IPSL, which is funded by the ANR (grant no. ANR-10-LABX-0018). This work has also received funding from the European Union's Horizon 2020 (H2020) research and innovation programme through the EUROCHAMP-2020 Infrastructure Activity under grant agreement No 730997. The authors thank K. Kandler, D. Seibert, and the LISA staff who collected the soil samples used in this study, E. Journet who provided the kaolinite sample, A. Petzold for helpful discussions on the aethalometer multiple scattering effects, and B. Tamime-Roussel for logistic help with the MAAP. The three anonymous reviewers are also gratefully acknowledged for their helpful comments which allowed improving and clarifying the manuscript.

References

Anderson, T. L. and Ogren, J. A.: Determining aerosol radiative properties using the TSI 3563 integrating nephelometer, Aerosol Sci. Technol., 29, 57–69, 1998.

Andreae, M. O. and Gelencsér, A.: Black Carbon or Brown Carbon? The Nature of Light-Absorbing Carbonaceous Aerosols. Atmos. Chem. Phys. 6:3131–3148, 2006.

Arnott, W. P., Hamasha, K., Moosmüuller, H., Sheridan, P. J., and Ogren, J. A.: Towards aerosol light-absorption measurements with a 7-wavelength aethalometer: Evaluation with a photoacoustic instrument and 3-wavelength nephelometer, Aerosol Sci. Tech., 39, 17–29, 2005.

Backman, J., Schmeisser, L., Virkkula, A., Ogren, J. A., Asmi, E., Starkweather, S., Sharma, S., Eleftheriadis, K., Uttal, T., Jefferson, A., Bergin, M., and Makshtas, A.: On Aethalometer measurement uncertainties and multiple scattering enhancement in the Arctic, Atmos. Meas. Tech. Discuss., doi:10.5194/amt-2016-294, in review, 2016.

Balkanski, Y., Schulz, M., Claquin, T., and Guibert, S.: Reevaluation of Mineral aerosol radiative forcings suggests a better agreement with satellite and AERONET data, Atmos. Chem. Phys., 7, 81–95, doi:10.5194/acp-7-81-2007, 2007.

Bauer, H., Schueller, E., Weinke, G., Berger, A., Hitzenberger, R., Marr, I. L., and Puxbaum, H.: Significant contributions of fungal spores to the organic carbon and to the aerosol mass balance of the urban atmospheric aerosol, Atmos. Environ., 42, 5542-5549, 2008.

Bergstrom, R. W., Pilewskie, P., Russell, P. B., Redemann, J., Bond, T. C., Quinn, P. K., and Sierau, B.: Spectral absorption properties of atmospheric aerosols, Atmos. Chem. Phys., 7, 5937-5943, doi:10.5194/acp-7-5937-2007, 2007.

Caponi, L., Formenti, P., Massabó, D., Di Biagio, C., Cazaunau, M., Pangui, E., Chavailler, S., Landrot, G., Fonda, E., Andreae', M. O., Kandler, K., Piketh, S., Saeed, T., Seibert, D., Williams, E., Balkanski, Y., Prati, P., and Doussin, J.-F.: Spectral- and size-resolved shortwave mass absorption cross-sections of mineral dust aerosols: a smog chamber study, Atmos. Chem. Phys., 17, 7175-7191, https://doi.org/10.5194/acp-17-7175-2017, 2017.

550 Cattrall, C., Carder, K. L., and Gordon, H. R.: Columnar aerosol single-scattering albedo and phase
551 function retrieved from sky radiance over the ocean: measurements of Saharan dust, J. Geophys.
552 Res., 108(D9), 4287, doi:10.1029/2002JD002497, 2003.

553 Collaud Coen, M., Weingartner, E., Apituley, A., Ceburnis, D., Fierz-Schmidhauser, R., Flentje, H.,
554 Henzing, J. S., Jennings, S. G., Moerman, M., Petzold, A., Schmid, O., and Baltensperger, U.:
555 Minimizing light absorption measurement artifacts of the Aethalometer: evaluation of five correction
556 algorithms, Atmos. Meas. Tech., 3, 457–474, doi:10.5194/amt-3-457-2010, 2010.

557 DeCarlo, P., Worsnop, D. R., Slowik, J. G., Davidovits, P., and Jimenez, J. L.: Particle Morphology
558 and Density Characterization by Combined Mobility and Aerodynamic Diameter Measurements. Part
559 1: Theory, Aerosol Sci. Technol., 38(12), 1185-1205, 2004.

560 Denjean, C., Formenti, P., Desboeufs, K., Chevaillier, S., Triquet, S., Maillé, M., Cazaunau, M.,
561 Laurent, B., Mayol-Bracero, O. L., Vallejo, P., Quiñones, M., Gutierrez-Molina, I. E., Cassola, F.,
562 Prati, P., Andrews, E., and Ogren, J.: Size distribution and optical properties of African mineral dust
563 after intercontinental transport, J. Geophys. Res. Atmos., 121, 7117–7138,
564 doi:10.1002/2016JD024783, 2016a.

565 Denjean, C., Cassola, F., Mazzino, A., Triquet, S., Chevaillier, S., Grand, N., Bourrianne, T.,
566 Momboisse, G., Sellegri, K., Schwarzenbock, A., Freney, E., Mallet, M., and Formenti, P.: Size
567 distribution and optical properties of mineral dust aerosols transported in the western Mediterranean,
568 Atmos. Chem. Phys., 16, 1081-1104, doi:10.5194/acp-16-1081-2016, 2016b.

569 Di Biagio, C., di Sarra, A., and Meloni, D.: Large atmospheric shortwave radiative forcing by
570 Mediterranean aerosols derived from simultaneous ground-based and spaceborne observations and
571 dependence on the aerosol type and single scattering albedo, J. Geophys. Res., 115, D10209, doi:
572 10.1029/2009JD012697, 2010.

573 Di Biagio, C., Formenti, P., Styler, S. A., Pangui, E., and Doussin, J.-F.: Laboratory chamber
574 measurements of the longwave extinction spectra and complex refractive indices of African and
575 Asian mineral dusts, Geophys. Res. Lett., 41, 6289-6297, doi:10.1002/2014GL060213, 2014.

576 Di Biagio, C., Formenti, P., Doppler, L., Gaimoz, C., Grand, N., Ancellet, G., Attié, J.-L., Bucci, S.,
577 Dubuisson, P., Fierli, F., Mallet, M., and Ravetta, F.: Continental pollution in the Western
578 Mediterranean basin: large variability of the aerosol single scattering albedo and influence on the
579 direct shortwave radiative effect, Atmos. Chem. Phys., 16, 10591-10607, doi:10.5194/acp-16-10591-
580 2016, 2016.

581 Di Biagio, C., Formenti, P., Balkanski, Y., Caponi, L., Cazaunau, M., Pangui, E., Journet, E., Nowak,
582 S., Caquineau, S., Andreae', M. O., Kandler, K., Saeed, T., Piketh, S., Seibert, D., Williams, E., and
583 Doussin, J.-F.: Global scale variability of the mineral dust longwave refractive index: a new dataset
584 of in situ measurements for climate modelling and remote sensing, Atmos. Chem. Phys., 17, 1901-
585 1929, doi:10.5194/acp-17-1901-2017, 2017.

586 di Sarra, A., C. Di Biagio, D. Meloni, F. Monteleone, G. Pace, S. Pugnaghi, and D. Sferlazzo,
587 Shortwave and longwave radiative effects of the intense Saharan dust event of March 25-26, 2010,
588 at Lampedusa (Mediterranean sea), J. Geophys. Res., 116, D23209, doi:10.1029/2011JD016238,
589 2011.

590 Egan, W. G. and Hilgeman, T. W.: Optical Properties of Inhomogeneous Materials: Applications to
591 Geology, Astronomy, Chemistry, and Engineering, Academic Press, 235 pp, 1979.

592 Engelbrecht, J. P., Moosmüller, H., Pincock, S., Jayanty, R. K. M., Lersch, T., and Casuccio, G.:
593 Technical note: Mineralogical, chemical, morphological, and optical interrelationships of mineral dust
594 re-suspensions, Atmos. Chem. Phys., 16, 10809-10830, doi:10.5194/acp-16-10809-2016, 2016.

595 Fialho, P., Hansenb, A. D. A., and Honrath, R. E.: Absorption coefficients by aerosols in remote
596 areas: a new approach to decouple dust and black carbon absorption coefficients using seven-
597 wavelength Aethalometer data, Aerosol Sci., 36, 267–282, 2005.

598 Formenti, P., Rajot, J. L., Desboeufs, K., Said, F., Grand, N., Chevaillier, S., and Schmechtig, C.:
599 Airborne observations of mineral dust over western Africa in the summer Monsoon season: spatial
600 and vertical variability of physico-chemical and optical properties, Atmos. Chem. Phys., 11, 6387-
601 6410, doi:10.5194/acp-11-6387-2011, 2011.

602 Goudie A. S., and Middleton, N. J.: Desert dust in the global system. Springer, Berlin, Heidelberg,

603 New York, 2006.

604 Hansen, A. D. A., Rosen, H., and Novakov, T.: The aethalometer—an instrument for the real-time
605 measurement of optical absorption by aerosol particles. The Science of the Total Environment, 36,
606 191–196, 1984.

607 Harrison, R. M., Yin, J., Mark, D., Stedman, J., Appleby, R.S., Booker, J., and Moorcroft, S.: Studies
608 of the coarse particle (2.5–10 μm) component in UK urban atmospheres, Atmos. Environ., 35,
609 3667–3679, 2001.

610 Heim, M., Mullins, B. J., Umhauer, H., and Kasper, G.: Performance evaluation of three optical
611 particle counters with an efficient "multimodal" calibration method, J. Aerosol Sci., 39, 1019–1031,
612 2008.

613 Heinold, B., I. Tegen, K. Schepanski, and O. Hellmuth, Dust radiative feedback on Saharan boundary
614 layer dynamics and dust mobilization, Geophys. Res. Lett., 35, L20817,
615 doi:10.1029/2008GL035319, 2008.

616 Highwood, E. J. and Ryder, C. L.: Radiative Effects of Dust, in: Mineral Dust: A Key Player in the
617 Earth System, edited by: Knippertz, P. and Stuut, J.-B. W., Springer ScienceCBusiness Media,
618 Dordrecht, https://doi.org/10.1007/978-94-017-8978-3_11, 2014.

619 Horvath, H.: Atmospheric Light Absorption - A Review, Atmos. Environ., 27A(3), 293-317, 1993.

620 Jin, Q., Zang, Z.-L., and Wei, J.: High sensitivity of Indian summer monsoon to Middle East dust
621 absorptive properties, Sci. Rep, 6:30690, doi: 10.1038/srep30690, 2016.

622 Kandler, K., Schütz, L., Deutscher, C., Ebert, M., Hofmann, H., Jäckel, S., Jaenicke, R., Knippertz, P.,
623 Lieke, K., Massling, A., Petzold, A., Schladitz, A.,Weinzierl, B.,Wiedensohler, A., Zorn, S., and
624 Weinbruch, S.: Size distribution, mass concentration, chemical and mineralogical composition and
625 derived optical parameters of the boundary layer aerosol at Tinfou, Morocco, during SAMUM 2006,
626 Tellus B, 61, 32–50, doi:10.1111/j.1600-0889.2008.00385.x, 2009.

627 Lack, D. A., Cappa, C. D., Covert, D. S., Baynard, T., Massoli, P., Sierau, B., Bates, T. S., Quinn, P.
628 K., Lovejoy, E. R., and Ravishankara, A. R.: Bias in Filter-Based Aerosol Light Absorption
629 Measurements Due to Organic Aerosol Loading: Evidence from Ambient Measurements, Aerosol
630 Sci. Tech., 42, 1033-1041, 2008.

631 Liu, X. J., and Harrison, R. M.: Properties of coarse particles in the atmosphere of the United
632 Kingdom, Atmos. Environ., 45, 3267–3276, 2011.

633 Mallet, M., Tulet, P., Serça, D., Solmon, F., Dubovik, O., Pelon, J., Pont, V., and Thouron, O.: Impact
634 of dust aerosols on the radiative budget, surface heat fluxes, heating rate profiles and convective
635 activity over West Africa during March 2006, Atmos. Chem. Phys., 9, 7143-7160, doi:10.5194/acp-9-
636 7143-2009, 2009.

637 Massoli, P., Kebabian, P. L., Onasch, T. B., Hills, F. B., and Freedman, A.: Aerosol Light Extinction
638 Measurements by Cavity Attenuated Phase Shift (CAPS) Spectroscopy: Laboratory Validation and
639 Field Deployment of a Compact Aerosol Particle Extinction Monitor, Aerosol Sci. Technol., 44, 428–
640 435, doi:10.1080/02786821003716599, 2010.

641 Miller, R.L., I. Tegen, and J.P. Perlwitz: Surface radiative forcing by soil dust aerosols and the
642 hydrologic cycle. J. Geophys. Res., 109, D04203, doi:10.1029/2003JD004085, 2004.

643 Miller, R.L., Knippertz, P., Pérez García-Pando, C., Perlwitz, J. P., and Tegen, I.: Impact of dust
644 radiative forcing upon climate. In Mineral Dust: A Key Player in the Earth System. P. Knippertz, and
645 J.-B.W. Stuut, Eds. Springer, 327-357, doi:10.1007/978-94-017-8978-3_13, 2014.

646 Moosmüller, H., and Arnott, W. P.: Particle Optics in the Rayleigh Regime, J. Air & Waste Manage.
647 Assoc., 59, 1028-1031, 2009.

648 Moosmüller, H., Chakrabarty, R. K., and Arnott, W. P.: Aerosol Light Absorption: A Review, J. Quant.
649 Spectr. Rad. Transf., 110(11), 844-878, 2009.

650 Müller, T., Henzing, J. S., de Leeuw, G., Wiedensohler, A., Alastuey, A., Angelov, H., Bizjak, M.,
651 Collaud Coen, M., Engström, J. E., Gruening, C., Hillamo, R., Hoffer, A., Imre, K., Ivanow, P.,
652 Jennings, G., Sun, J. Y., Kalivitis, N., Karlsson, H., Komppula, M., Laj, P., Li, S.-M., Lunder, C.,
653 Marinoni, A., Martins dos Santos, S., Moerman, M., Nowak, A., Ogren, J. A., Petzold, A., Pichon, J.

M., Rodriquez, S., Sharma, S., Sheridan, P. J., Teinilä, K., Tuch, T., Viana, M., Virkkula, A., Weingartner, E., Wilhelm, R., and Wang, Y. Q.: Characterization and intercomparison of aerosol absorption photometers: result of two intercomparison workshops, Atmos. Meas. Tech., 4, 245-268, doi:10.5194/amt-4-245-2011, 2011.

Pakbin, P., Hudda, N., Cheng, K. L., Moore, K. F., Sioutas, C.: Spatial and temporal variability of coarse ($PM_{10-2.5}$) particulate matter concentrations in the Los Angeles area, Aerosol Sci. Technol., 44, 514–525, 2010.

Perez, C., Nickovic, S., Baldasano, J. M., Sicard, M., Rocadenbosch, F., and Cachorro, V. E.: A long Saharan dust event over the western Mediterranean: Lidar, Sun photometer observations, and regional dust modeling, J. Geophys. Res., 111, D15214, doi:10.1029/2005JD006579, 2006.

Petzold, A., and Schönlinner, M.: Multiangle Absorption Photometry–A New Method for the Measurement of Aerosol Light Absorption and Atmospheric Black Carbon, J. Aerosol Sci., 35:421–441, 2004.

Petzold, A., Schloesser, H., Sheridan, P. J., Arnott, W. P., Ogren, J. A., and Virkkula, A.: Evaluation of Multi-angle Absorption Photometry for Measuring Aerosol Light Absorption, Aerosol Sci. Technol., 39, 40–51, 2005.

Querol, X., Pey, J., Pandolfi, M., Alastuey, A., Cusack, M., Pérez, N., Moreno, T., Viana, M., Mihalopoulos, N., Kallos, G., and Kleanthous, S.: African dust contributions to mean ambient PM10 mass-levels across the Mediterranean Basin, Atmos. Environ., 43, 4266-4277, 2009.

Reddy, M. S., O. Boucher, Y. Balkanski, and M. Schulz: Aerosol optical depths and direct radiative perturbations by species and source type. Geophys. Res. Lett., 32, L12803, 2005.

Redmond, H. E., Dial, K. D., and Thompson, J. E.: Light scattering and absorption by wind blown dust: Theory, measurement, and recent data, Aeolian Res., 2, 5–26, 2010.

Ryder, C. L., Highwood, E. J., Rosenberg, P. D., Trembath, J., Brooke, J. K., Bart, M., Dean, A., Crosier, J., Dorsey, J., Brindley, H., Banks, J., Marsham, J. H., McQuaid, J. B., Sodemann, H., and Washington, R.: Optical properties of Saharan dust aerosol and contribution from the coarse mode as measured during the Fennec 2011 aircraft campaign, Atmos. Chem. Phys., 13, 303-325, doi:10.5194/acp-13-303-2013, 2013.

Sandradewi, J., Prévôt, A. S. H., Weingartner, E., Schmidhauser, R., Gysel, M., and Baltensperger, U.: A study of wood burning and traffic aerosols in an Alpine valley using a multi-wavelength Aethalometer, Atmos. Environ., 42, 101-112, 2008.

Saturno, J., Pöhlker, C., Massabò, D., Brito, J., Carbone, S., Cheng, Y., Chi, X., Ditas, F., Hrabě de Angelis, I., Morán-Zuloaga, D., Pöhlker, M. L., Rizzo, L. V., Walter, D., Wang, Q., Artaxo, P., Prati, P., and Andreae, M. O.: Comparison of different Aethalometer correction schemes and a reference multi-wavelength absorption technique for ambient aerosol data, Atmos. Meas. Tech. Discuss., doi:10.5194/amt-2016-361, in review, 2016.

Schladitz, A., Müller, T., Kaaden, N., Massling, A., Kandler, K., Ebert, M., Weinbruch, S., Deutscher, C., and Wiedensohler, A.: In situ measurements of optical properties at Tinfou (Morocco) during the Saharan Mineral Dust Experiment SAMUM 2006, Tellus B, 61, 64–78, doi:10.1111/j.1600-0889.2008.00397.x, 2009.

Schmid, O., Artaxo, P., Arnott,W. P., Chand, D., Gatti, L. V., Frank, G. P., Hoffer, A., Schnaiter, M., and Andreae, M. O.: Spectral light absorption by ambient aerosols influenced by biomass burning in the Amazon Basin. I: Comparison and field calibration of absorption measurement techniques, Atmos. Chem. Phys., 6, 3443–3462, 2006.

Segura, S., Estellés, V., Titos, G., Lyamani, H., Utrillas, M. P., Zotter, P., Prévôt, A. S. H., Močnik, G., Alados-Arboledas, L., and Martínez-Lozano, J. A., Determination and analysis of in situ spectral aerosol optical properties by a multi-instrumental approach, Atmos. Meas. Tech., 7, 2373-2387, doi: 10.5194/amt-7-2373-2014, 2014.

Sherman, J. P., Sheridan, P. J., Ogren, J. A., Andrews, E., Hageman, D., Schmeisser, L., Jefferson, A., and Sharma, S.: A multi-year study of lower tropospheric aerosol variability and systematic relationships from four North American regions, Atmos. Chem. Phys., 15, 12487-12517, doi:10.5194/acp-15-12487-2015, 2015.

706 Slingo, A., et al., Observations of the impact of a major Saharan dust storm on the atmospheric
707 radiation balance, Geophys. Res. Lett., 33, L24817, doi:10.1029/2006GL027869, 2006.

708 Sokolik, I., and Toon, O.: Incorporation of mineralogical composition into models of the radiative
709 properties of mineral aerosol from UV to IR wavelengths, J. Geophys. Res., 104, 9423-9444, 1999.

710 Solmon, F., Mallet, M., Elguindi, N., Giorgi, F., Zakey, A. and Konaré, A.: Dust aerosol impact on
711 regional precipitation over western Africa, mechanisms and sensitivity to absorption properties,
712 Geophys. Res. Lett., 35, L24705, doi:10.1029/2008GL035900, 2008.

713 Toon, O. B., Pollack, J. B., and Khare, B. N.: The Optical Constants of Several Atmospheric Aerosol
714 Species: Ammonium Sulfate, Aluminum Oxide, and Sodium Chloride, J. Geophys. Res., 81, 5733–
715 5748, 1976.

716 Utry, N., Ajtai, T., Pintér, M., Tombácz, E., Illés, E., Bozóki, Z., and Szabó, G.: Mass-specific optical
717 absorption coefficients and imaginary part of the complex refractive indices of mineral dust
718 components measured by a multi-wavelength photoacoustic spectrometer, Atmos. Meas. Tech., 8,
719 401-410, doi:10.5194/amt-8-401-2015, 2015.

720 Utry, N., Ajtai, T., Pintér, M. Illés, E., Tombácz, E., Szabó, G., and Bozóki, Z.: Generation and UV-
721 VIS-NIR spectral responses of organo-mineral aerosol for modelling soil derived dust, Atmos.
722 Environ., 152, 553-561, 2017.

723 Virkkula, A., Makela, T., Hillamo, R., Yli-Tuomi, T., Hirsikko, A., Hameri, K., and Koponen, I. K.: A
724 simple procedure for correcting loading effects of aethalometer data, J. Air Waste Manage., 57(10),
725 1214–1222, 2007.

726 von der Weiden, S.-L., Drewnick, F., and Borrmann, S.: Particle Loss Calculator – a new software tool
727 for the assessment of the performance of aerosol inlet systems, Atmos. Meas. Tech., 2, 479–494,
728 2009.

729 Weingartner, E., Saathof, H., Schnaiter, M., Streit, N., Bitnar, B., and Baltensperger, U.: Absorption of
730 light by soot particles: Determination of the absorption coefficient by means of Aethalometers, J.
731 Aerosol Sci., 34, 1445–1463, 2003.

732 Yoshioka, M., N.M.Mahowald, A. J. Conley,W. D. Collins, D.W. Fillmore, C. S. Zender, and D. B.
733 Coleman: Impact of desert dust radiative forcing on sahel precipitation: Relative importance of dust
734 compared to sea surface temperature variations, vegetation changes, and greenhouse gas
735 warming, J. Clim., 20, 1445– 1467, 2007.

Table captions

Table 1. Specifications and references of instruments used during experiments.

Table 2. Summary of experiments and results. The mean and the standard deviation of $D_{eff,fine}$, $D_{eff,coarse}$, SSA at 450 and 660 nm, C_{ref}^{*}, C_{ref}(W2003), and C_{ref}(C2010) are reported. As a reminder: C_{ref}^{*} is the multiple scattering correction obtained not taking into account the loading effect correction in aethalometer data; C_{ref}(W2003) and C_{ref}(C2010) take the loading effect correction into account, by using the parametrisations by Weingartner et al. (2003) (referred as W2003) and Collaud Coen et al. (2010) (referred as C2010), respectively. The maximum of the % difference between C_{ref}^{*}, C_{ref}(W2003), and C_{ref}(C2010) is indicated in the table.

Table 3. Mean and standard deviation multiple scattering correction $\overline{C_{ref}}$ at 450 and 660 nm for dust, kaolinite, and ambient air. The $\overline{C_{ref}}$ was calculated as the mean of the C_{ref}^{*}, C_{ref}(W2003), and C_{ref}(C2010) obtained at each wavelength for the different aerosol types. As a reminder: C_{ref}^{*} is the multiple scattering correction obtained not taking into account the loading effect correction in aethalometer data; C_{ref}(W2003) and C_{ref}(C2010) take the loading effect correction into account, by using the parametrisations by Weingartner et al. (2003) and Collaud Coen et al. (2010), respectively.

Figure captions

Figure 1. Experimental setup used for the aethalometer intercomparison experiments.

Figure 2. Temporal series of experiments showing the measured optical data at 660 nm. The different panels show (from the top to the bottom): (i) the loading-corrected aethalometer attenuation at 660 nm (data corrected with the R formulation by Collaud Coen et al. (2010) (referred to as R(C2010)) are shown) and the MAAP aerosol absorption coefficient; (ii) the aerosol extinction at 660 nm extrapolated from CAPS PMex measurements and estimated as the sum of nephelometer scattering and MAAP absorption; (iii) the extinction aerosol Ángstrom exponent; (iv) the aerosol single scattering albedo at 660 nm. Each point in the plot corresponds to 2 min average data. The x-axis indicates the data point sequential number. Experiments with dust samples and kaolinite occurred between the 3rd and the 9th of November 2016 and lasted between 1 and 2 hours each. Ambient air data were collected at different steps between the 8th and the 14th November 2016 for a total of 7 hours of measurements.

Figure 3. Ammonium sulfate experiment. Left panel: temporal evolution of the extinction and scattering coefficients measured by the CAPS PMex and the nephelometer at 450 nm (blue scale) and 630 nm (red scale). Each point in the plot corresponds to 2 min average data. Right panel: CAPS PMex versus nephelometer data (10 minutes averages). The y=x line and the results of the linear fit between CAPS and nephelometer data are also shown in the plot.

Figure 4. CAPS PMex extinction coefficient extrapolated at 660 nm versus nephelometer+MAAP calculated extinction at 660 nm for all experiments (dust, kaolinite, ambient air). Each point in the plot

corresponds to 10 min average data. The y=x line and the results of the linear fit between CAPS and nephelometer+MAAP data are also shown in the plot.

Figure 5. Left panel: estimated f values versus (1-SSA) at 660 nm for dust aerosols. Different symbols are used to distinguish between dust from different sources. The uncertainty of (1-SSA) is the standard deviation over 2-min data, while that of f is calculated with the error propagation formula taking into account the uncertainty of *a* (±0.14) and that of (1-SSA). Right panel: f versus SSA at 660 nm for all experiments. Different symbols are used to distinguish between different aerosol types. The results of the linear fit between f and (1-SSA) are also reported. Data from Weingartner et al. (2003) (W2003) (extracted from their Figure 4) are also shown in the plot for comparison.

Figure 6. Top panel: C_{ref}(W2003) (multiple scattering correction obtained by taking into account the loading effect correction using the parametrisations by Weingartner et al. (2003)) versus SSA at 450 and 660 nm for mineral dust samples analysed in this study. Different symbols are used to distinguish between dust from different sources. As indicated in Table 2, the difference between C_{ref}^{*}, C_{ref}(W2003), and C_{ref}(C2010) is very low for mineral dust aerosols. The uncertainty of SSA is the standard deviation over 2-min data, while that of C_{ref}(W2003) is calculated with the error propagation formula taking into account the uncertainty of $\beta_{abs,ref}$ and that of β_{ATT}/R(W2003). Bottom panel: C_{ref} versus SSA at 450 and 660 nm for the different aerosol samples analysed in this study. Different symbols are used to distinguish between different aerosol types. Data for both C_{ref}(W2003) and C_{ref}^{*} (multiple scattering correction obtained not taking into account the loading effect correction in aethalometer data) are shown for ambient air aerosols, while for dust and kaolinite, for which the difference between the different formulations is very low, only C_{ref}(W2003) is reported. Data from Weigartner et al. (2003) (W2003) (C_{ref} from their Table 3, and SSA extracted from their Fig. 4) and Collaud Coen et al. (2010) (C2010) (extracted from their Fig. 5) at 660 nm are also shown in the plot for comparison. The results of the linear fits between C_{ref} and SSA for mineral dust and for the entire dataset are also shown in the plot.

Figure 7. Examples of number size distribution (normalised to the total number concentration) for ammonium sulfate, dust (Niger sample), kaolinite, and ambient air aerosols. Data refer to the mean over each experiment as measured from the SMPS and the OPC. Error bars (standard deviations) have been omitted for the sake of clarity.

Figure 8. Top panel: C_{ref}(W2003) (multiple scattering correction obtained by taking into account the loading effect correction using the parametrisations by Weingartner et al. (2003)) at 450 and 660 nm versus the effective diameter coarse $D_{eff,coarse}$. for mineral dust samples analysed in this study. Different symbols are used to distinguish between dust from different sources. The uncertainty of $D_{eff,coarse}$ is the standard deviation over 2-min data, while that of C_{ref}(W2003) is calculated with the error propagation formula taking into account the uncertainty of $\beta_{abs,ref}$ and that of β_{ATT}/R(W2003). Bottom panel: C_{ref} at 450 and 660 nm versus the effective diameter coarse $D_{eff,coarse}$ for the different aerosol samples analysed in this study. Different symbols are used to distinguish between different aerosol types. Data for both C_{ref}(W2003) and C_{ref}^{*} (multiple scattering correction obtained not taking into account the loading effect correction in aethalometer data) are shown for ambient air aerosols,

811 while for dust and kaolinite, for which the difference between the different formulations is very low,
812 only C_{ref}(W2003) is reported. The results of the linear fits between C_{ref} and $D_{eff,coarse}$ for mineral dust
813 and for the entire dataset are also shown in the plot.

814

815 **Table 1.** Specifications and references of instruments used during experiments.

Instrument	Property	Operating wavelength (nm)	Time resolution	Flowrate (L min^{-1})	Percent uncertainty	Reference
Aethalometer (model AE-31, Magee Sci.)	Spectral absorption coefficient	370, 470, 520, 590, 660, 880, 950	2 min	8	±20% (attenuation coefficient)	Hansen et al. (1984) ; W2003 ; C2010
Multi-Angle Absorption Photometer (MAAP, model 5012, Thermo Sci.)	Single-wavelength absorption coefficient	670	1 min	8	±12%	Petzold and Schönlinner (2004); Petzold et al. (2005)
Cavity Attenuated Phase Shift Extinction (CAPS PMex, Aerodyne)	Spectral extinction coefficient	450, 630	1 s	0.85	±5%	Massoli et al. (2010)
Nephelometer (model 3563, TSI Inc.)	Spectral scattering coefficient	450, 550, 700	1 s	18	±~9%	Sherman et al. (2015)
SMPS (DMA model 3080, CPC model 3772, TSI Inc.)	Number size distribution	–	3 min	2	–	De Carlo et al. (2004)
OPC optical particle counter (model 1.109, Grimm Inc.)	Number size distribution	655	6 s	1.2	±15% (diameter optical to geometric conversion); ±10 (concentration)	Heim et al. (2008)

816

817

818 **Table 2**. Summary of experiments and results. The mean and the standard deviation of $D_{eff,fine}$,
819 $D_{eff,coarse}$, SSA at 450 and 660 nm, C_{ref}^{*}, C_{ref}(W2003), and C_{ref}(C2010) are reported. As a reminder:
820 C_{ref}^{*} is the multiple scattering correction obtained not taking into account the loading effect correction
821 in aethalometer data; C_{ref}(W2003) and C_{ref}(C2010) take the loading effect correction into account, by
822 using the parametrisations by Weingartner et al. (2003) (referred as W2003) and Collaud Coen et al.
823 (2010) (referred as C2010), respectively. The maximum of the % difference between C_{ref}^{*},
824 C_{ref}(W2003), and C_{ref}(C2010) is indicated in the table.

Aerosol ID	**Source**	**$D_{eff,fine}$ (µm)** **$D_{eff,coarse}$ (µm)**	**SSA** ***450 nm*** **660 nm**	**C_{ref}^{*}** ***450 nm*** **660 nm**	**C_{ref} (W2003)** ***450 nm*** **660 nm**	**C_{ref} (C2010)** ***450 nm*** **660 nm**	**Max % diff C_{ref}** ***450 nm*** **660 nm**
Ammonium sulfate	Sigma-Aldrich 99.999% purity	–	*0.999 ± (<)0.001* 0.999 ± (<)0.001		–	–	
Niger 1	Sahel (13.52°N, 2.63°E)	0.38 ± 0.01 2.6 ± 0.1	*0.93 ± 0.01* 0.98 ± 0.01	*2.00 ± 0.45* 1.87 ± 0.51	*2.01 ± 0.45* 1.87 ± 0.51	*2.02 ± 0.45* 1.88 ± 0.51	*1.0 %* 0.4 %
Niger 2	Sahel (13.52°N, 2.63°E)	0.32 ± 0.02 2.3 ± 0.1	*0.92 ± 0.01* 0.98 ± 0.01	*2.05 ± 0.46* 1.89 ± 0.57	*2.11 ± 0.47* 1.92 ± 0.56	*2.10 ± 0.47* 1.92 ± 0.57	*2.8 %* 1.6 %
China	Gobi desert (39.43°N, 105.67°E)	0.44 ± 0.01 3.1 ± 0.2	*0.94 ± 0.01* 0.98 ± 0.01	*2.15 ± 0.48* 2.02 ± 0.62	*2.16 ± 0.48* 2.01 ± 0.62	*2.16 ± 0.48* 2.02 ± 0.63	*0.5 %* 0.3 %
Arizona	Sonoran desert (33.15°N, 112.08°W)	0.53 ± 0.02 3.1 ± 0.2	*0.96 ± 0.01* 0.99 ± 0.01	*1.81 ± 0.40* 1.76 ± 0.56	*1.82 ± 0.41* 1.78 ± 0.55	*1.82 ± 0.41* 1.78 ± 0.57	*0.5 %* 1.1 %
Tunisia	Sahara desert (33.02°N, 10.67°E)	0.48 ± 0.03 3.2 ± 0.7	*0.96 ± 0.01* 0.99 ± 0.01	*1.97 ± 0.49* 1.80 ± 0.42	*1.98 ± 0.44* 1.80 ± 0.42	*1.98 ± 0.44* 1.80 ± 0.42	*0.5 %* 0 %
Australia	Strzelecki desert (31.33°S, 140.33°E)	0.55 ± 0.02 2.4 ± 0.1	*0.85 ± 0.01* 0.98 ± 0.01	*2.52 ± 0.56* 2.28 ± 0.74	*2.56 ± 0.57* 2.26 ± 0.72	*2.56 ± 0.57* 2.28 ± 0.74	*1.6 %* 0.9 %
Namibia	Namib desert (19.0°S, 13.0°E)	0.45 ± 0.04 3.6 ± 0.3	*0.95 ± 0.01* 0.98 ± 0.01	*2.02 ± 0.45* 1.75 ± 0.57	*2.03 ± 0.45* 1.76 ± 0.54	*2.03 ± 0.45* 1.79 ± 0.57	*0.5 %* 2.2 %
Kaolinite	Source Clay Repository KGa-2	0.39 ± 0.07 2.3 ± 1.6	*0.96 ± 0.01* 0.97 ± 0.01	*2.47 ± 0.55* 2.31 ± 0.60	*2.51 ± 0.56* 2.34 ± 0.60	*2.50 ± 0.56* 2.33 ± 0.60	*1.6 %* 1.3 %
Ambient air 1	Suburbs of Paris	0.24 ± 0.08 5.2 ± 0.9	*0.79 ± 0.05* 0.61 ± 0.08	*3.87 ± 0.87* 1.97 ± 0.71	*4.01 ± 0.90* 2.05 ± 0.73	*4.03 ± 0.90* 2.11 ± 0.76	*4.0 %* 6.6 %
Ambient air 2	Suburbs of Paris	0.50 ± 0.02 4.5 ± 0.1	*0.72 ± 0.04* 0.67 ± 0.09	*3.22 ± 0.72* 1.66 ± 0.44	*3.68 ± 0.82* 1.94 ± 0.52	*3.57 ± 0.80* 1.87 ± 0.50	*12.5 %* 14.4 %
Ambient air 3	Suburbs of Paris	0.46 ± 0.03 6.2 ± 0.7	*0.78 ± 0.06* 0.54 ± 0.10	*3.93 ± 0.88* 2.32 ± 0.76	*4.35 ± 0.97* 2.78 ± 0.89	*4.25 ± 0.95* 2.68 ± 0.87	*21.1 %* 16.5 %
Ambient air 4	Suburbs of Paris	0.53 ± 0.05 5.3 ± 1.3	*0.63 ± 0.05* 0.42 ± 0.08	*3.41 ± 0.76* 2.25 ± 0.68	*3.90 ± 0.87* 2.69 ± 0.81	*3.79 ± 0.85* 2.62 ± 0.79	*12.6 %* 16.4 %
Ambient air 5	Suburbs of Paris	0.37 ± 0.03 3.4 ± 0.1	*0.76 ± 0.08* 0.65 ± 0.12	*2.72 ± 0.61* 2.54 ± 0.82	*2.58 ± 0.58* 2.51 ± 0.81	*2.77 ± 0.62* 2.61 ± 0.85	*5.4 %* 2.7 %
Ambient air 6	Suburbs of Paris	0.37 ± 0.05 4.1 ± 1.0	*0.62 ± 0.04* 0.46 ± 0.09	*2.75 ± 0.50* 2.24 ± 0.60	*2.78 ± 0.62* 2.96 ± 0.79	*2.66 ± 0.59* 2.79 ± 0.75	*19.1 %* 24.3 %
Ambient air 7	Suburbs of Paris	0.40 ± 0.01 4.7 ± 0.7	*0.87 ± 0.05* 0.76 ± 0.08	*3.85 ± 0.86* 1.86 ± 0.74	*4.06 ± 0.91* 2.04 ± 0.69	*4.01 ± 0.90* 2.02 ± 0.80	*5.2 %* 8.8 %
Ambient air 8	Suburbs of Paris	0.42 ± 0.07 4.3 ± 0.7	*0.78 ± 0.06* 0.71 ± 0.07	*1.91 ± 0.43* 2.09 ± 0.61	*2.22 ± 0.50* 2.53 ± 0.73	*2.16 ± 0.48* 2.45 ± 0.72	*14.0 %* 17.4 %

825 **Table 3**. Mean and standard deviation multiple scattering correction $\overline{C_{ref}}$ at 450 and 660 nm for dust,
826 kaolinite, and ambient air. The $\overline{C_{ref}}$ was calculated as the mean of the C_{ref}^{*}, C_{ref}(W2003), and
827 C_{ref}(C2010) obtained at each wavelength for the different aerosol types. As a reminder: C_{ref}^{*} is the
828 multiple scattering correction obtained not taking into account the loading effect correction in
829 aethalometer data; C_{ref}(W2003) and C_{ref}(C2010) take the loading effect correction into account, by
830 using the parametrisations by Weingartner et al. (2003) and Collaud Coen et al. (2010), respectively.

831

	$\overline{C_{ref}}$	
	450 nm	**660 nm**
Mineral dust	2.09 ± 0.22	1.92 ± 0.17
Kaolinite	2.49 ± 0.02	2.31 ± 0.02
Ambient air	3.31 ± 0.75	2.32 ± 0.35

832

833

Figure 1. Experimental setup used for the aethalometer intercomparison experiments.

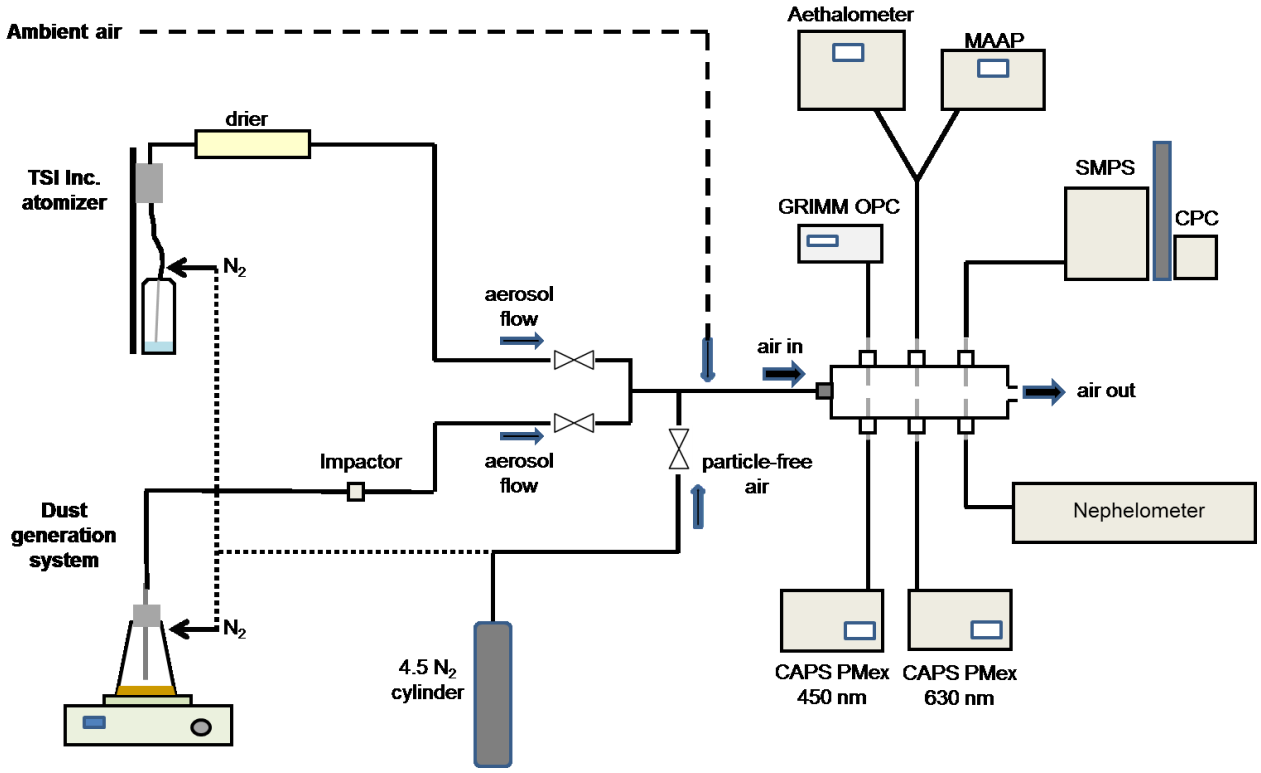

Figure 2. Temporal series of experiments showing the measured optical data at 660 nm. The different panels show (from the top to the bottom): (i) the loading-corrected aethalometer attenuation at 660 nm (data corrected with the R formulation by Collaud Coen et al. (2010) (referred to as R(C2010)) are shown) and the MAAP aerosol absorption coefficient; (ii) the aerosol extinction at 660 nm extrapolated from CAPS PMex measurements and estimated as the sum of nephelometer scattering and MAAP absorption; (iii) the extinction aerosol Ångstrom exponent; (iv) the aerosol single scattering albedo at 660 nm. Each point in the plot corresponds to 2 min average data. The x-axis indicates the data point sequential number. Experiments with dust samples and kaolinite occurred between the 3rd and the 9th of November 2016 and lasted between 1 and 2 hours each. Ambient air data were collected at different steps between the 8th and the 14th November 2016 for a total of 7 hours of measurements.

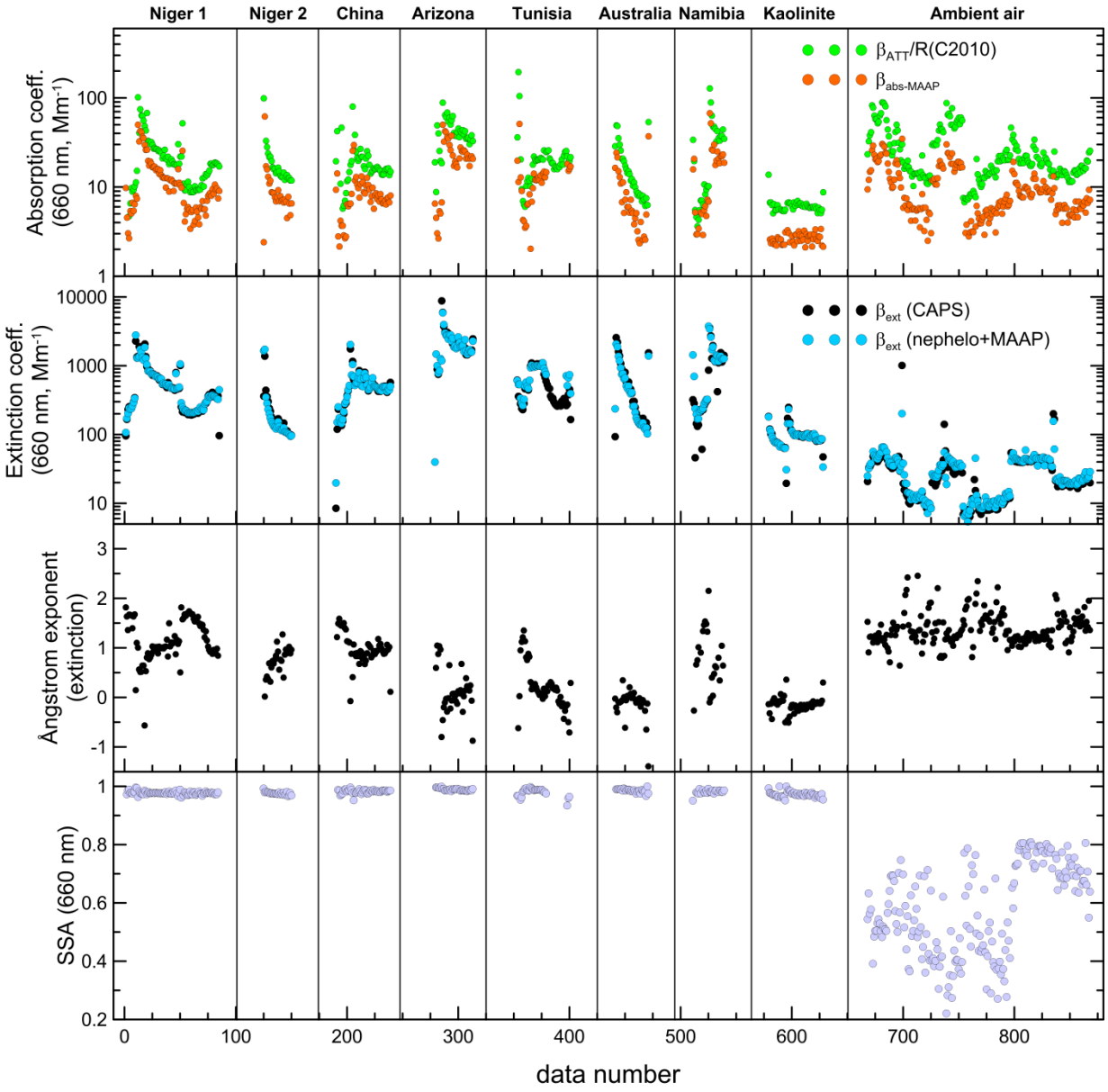

Figure 3. Ammonium sulfate experiment. Left panel: temporal evolution of the extinction and scattering coefficients measured by the CAPS PMex and the nephelometer at 450 nm (blue scale) and 630 nm (red scale). Each point in the plot corresponds to 2 min average data. Right panel: CAPS PMex versus nephelometer data (10 minutes averages). The y=x line and the results of the linear fit between CAPS and nephelometer data are also shown in the plot.

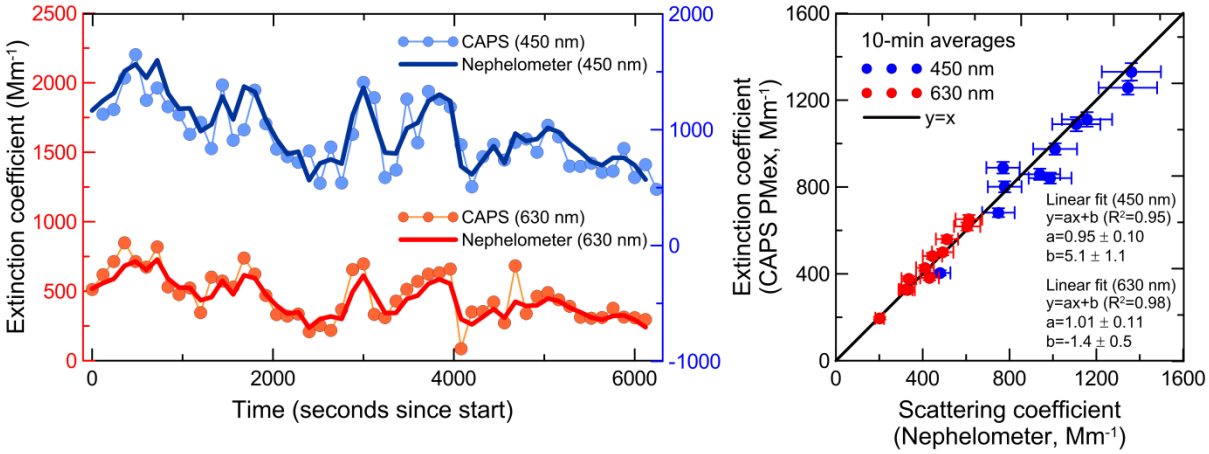

Figure 4. CAPS PMex extinction coefficient extrapolated at 660 nm versus nephelometer+MAAP calculated extinction at 660 nm for all experiments (dust, kaolinite, ambient air). Each point in the plot corresponds to 10 min average data. The y=x line and the results of the linear fit between CAPS and nephelometer+MAAP data are also shown in the plot.

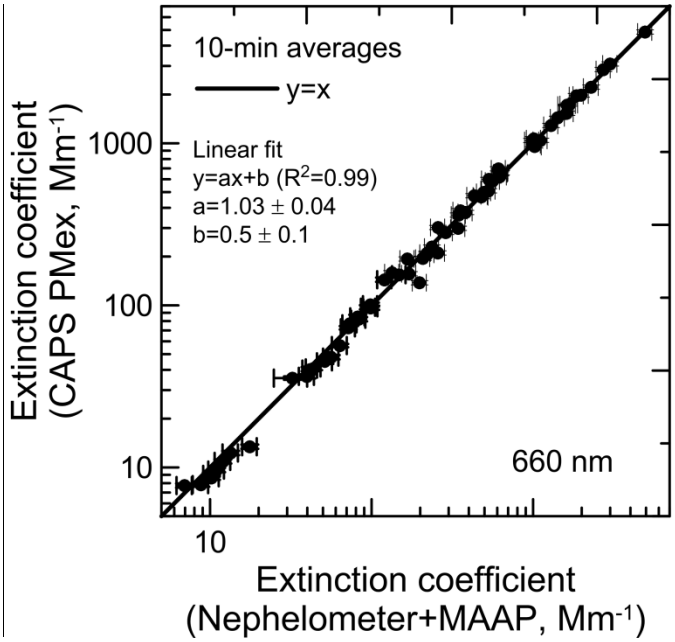

Figure 5. Left panel: estimated f values versus (1-SSA) at 660 nm for dust aerosols. Different symbols are used to distinguish between dust from different sources. The uncertainty of (1-SSA) is the standard deviation over 2-min data, while that of f is calculated with the error propagation formula taking into account the uncertainty of *a* (±0.14) and that of (1-SSA). Right panel: f versus SSA at 660 nm for all experiments. Different symbols are used to distinguish between different aerosol types. The results of the linear fit between f and (1-SSA) are also reported. Data from Weingartner et al. (2003) (W2003) (extracted from their Figure 4) are also shown in the plot for comparison.

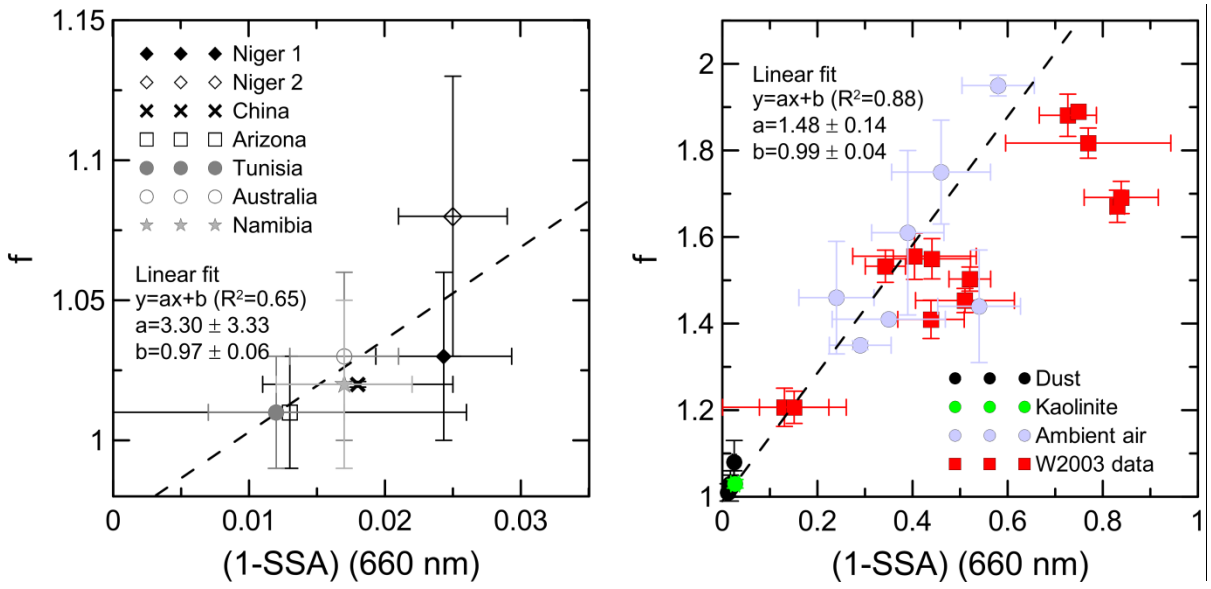

Figure 6. Top panel: C_{ref}(W2003) (multiple scattering correction obtained by taking into account the loading effect correction using the parametrisations by Weingartner et al. (2003)) versus SSA at 450 and 660 nm for mineral dust samples analysed in this study. Different symbols are used to distinguish between dust from different sources. As indicated in Table 2, the difference between C_{ref}^{*}, C_{ref}(W2003), and C_{ref}(C2010) is very low for mineral dust aerosols. The uncertainty of SSA is the standard deviation over 2-min data, while that of C_{ref}(W2003) is calculated with the error propagation formula taking into account the uncertainty of $\beta_{abs,ref}$ and that of β_{ATT}/R(W2003). Bottom panel: C_{ref} versus SSA at 450 and 660 nm for the different aerosol samples analysed in this study. Different symbols are used to distinguish between different aerosol types. Data for both C_{ref}(W2003) and C_{ref}^{*} (multiple scattering correction obtained not taking into account the loading effect correction in aethalometer data) are shown for ambient air aerosols, while for dust and kaolinite, for which the difference between the different formulations is very low, only C_{ref}(W2003) is reported. Data from Weigartner et al. (2003) (W2003) (C_{ref} from their Table 3, and SSA extracted from their Fig. 4) and Collaud Coen et al. (2010) (C2010) (extracted from their Fig. 5) at 660 nm are also shown in the plot for comparison. The results of the linear fits between C_{ref} and SSA for mineral dust and for the entire dataset are also shown in the plot.

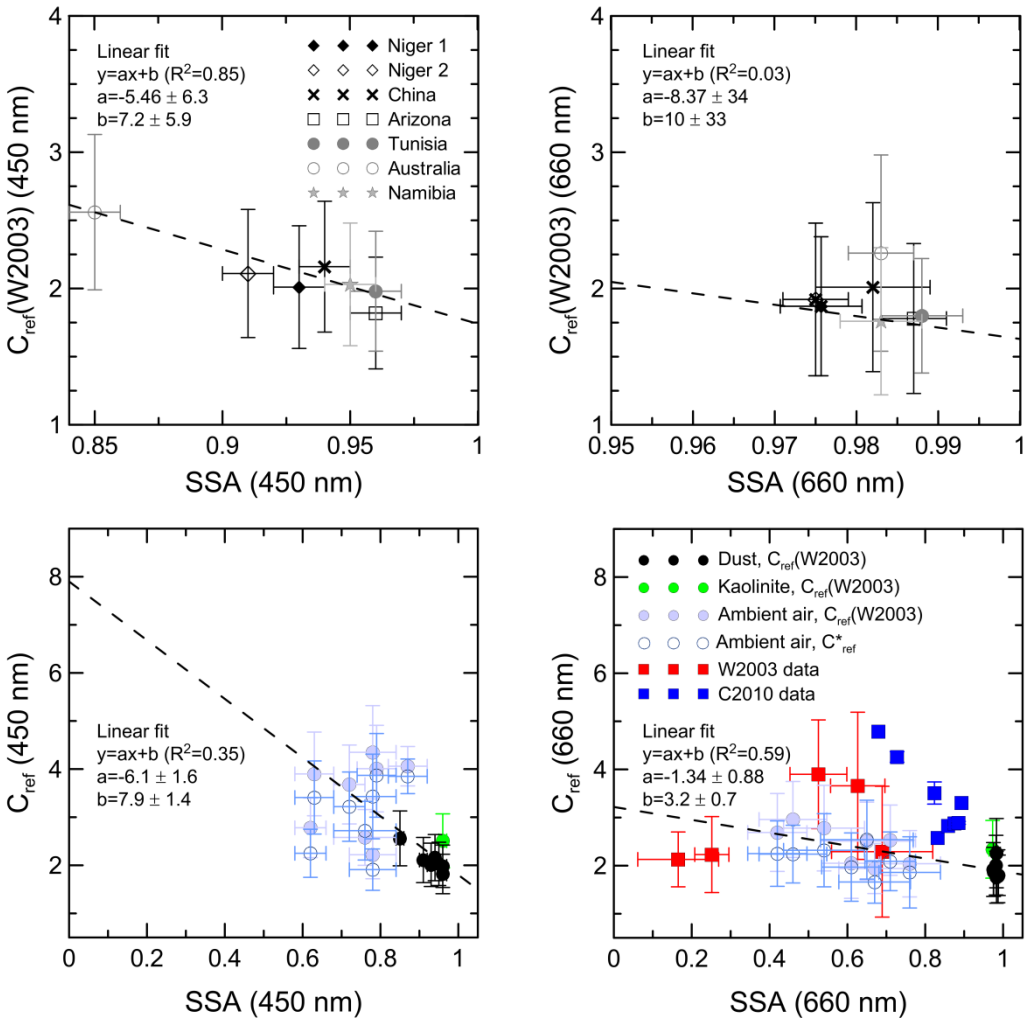

Figure 7. Examples of number size distribution (normalised to the total number concentration) for ammonium sulfate, dust (Niger sample), kaolinite, and ambient air aerosols. Data refer to the mean over each experiment as measured from the SMPS and the OPC. Error bars (standard deviations) have been omitted for the sake of clarity.

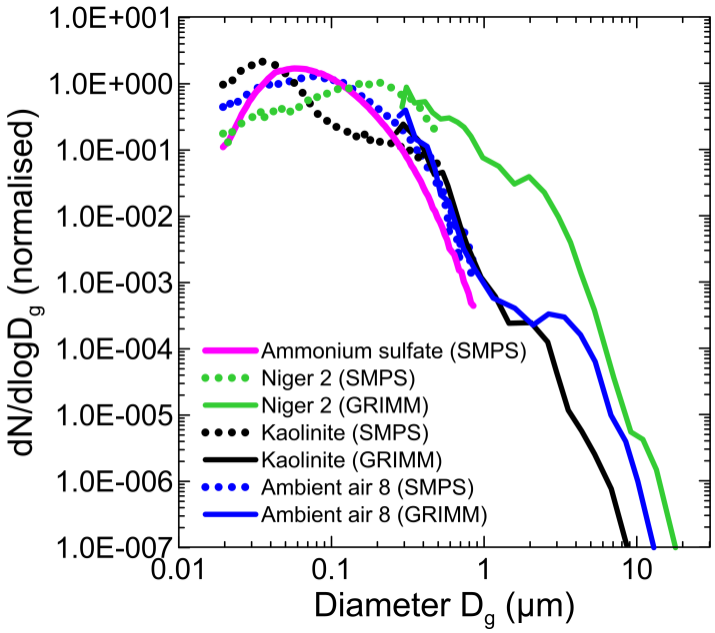

Figure 8. Top panel: C_{ref}(W2003) (multiple scattering correction obtained by taking into account the loading effect correction using the parametrisations by Weingartner et al. (2003)) at 450 and 660 nm versus the effective diameter coarse $D_{eff,coarse}$. for mineral dust samples analysed in this study. Different symbols are used to distinguish between dust from different sources. The uncertainty of $D_{eff,coarse}$ is the standard deviation over 2-min data, while that of C_{ref}(W2003) is calculated with the error propagation formula taking into account the uncertainty of $\beta_{abs,ref}$ and that of β_{ATT}/R(W2003). Bottom panel: C_{ref} at 450 and 660 nm versus the effective diameter coarse $D_{eff,coarse}$ for the different aerosol samples analysed in this study. Different symbols are used to distinguish between different aerosol types. Data for both C_{ref}(W2003) and C_{ref}^{*} (multiple scattering correction obtained not taking into account the loading effect correction in aethalometer data) are shown for ambient air aerosols, while for dust and kaolinite, for which the difference between the different formulations is very low, only C_{ref}(W2003) is reported. The results of the linear fits between C_{ref} and $D_{eff,coarse}$ for mineral dust and for the entire dataset are also shown in the plot.